

Modelling self-interacting dark matter substructures I: Calibration with N-body simulations of a Milky-Way-sized halo and its satellite

Masato Shirasaki^{1,2*}, Takashi Okamoto³, and Shin’ichiro Ando^{4,5}

¹*National Astronomical Observatory of Japan, Mitaka, Tokyo 181-8588, Japan*

²*The Institute of Statistical Mathematics, Tachikawa, Tokyo 190-8562, Japan*

³*Faculty of Science, Hokkaido University, N10 W8, Kitaku, Sapporo, Hokkaido 060-0810 Japan*

⁴*GRAPPA Institute, University of Amsterdam, 1098 XH Amsterdam, The Netherlands*

⁵*Kavli Institute for the Physics and Mathematics of the Universe (WPI), University of Tokyo, Chiba 277-8583, Japan*

23 May 2022

ABSTRACT

We study evolution of single subhaloes with their masses of $\sim 10^9 M_\odot$ in a Milky-Way-sized host halo for self-interacting dark matter (SIDM) models. We perform ideal dark-matter-only N-body simulations of halo-subhalo mergers by varying self-scattering cross sections (including a velocity-dependent scenario), subhalo orbits, and internal properties of the subhalo. We calibrate a gravothermal fluid model to predict time evolution in spherical mass density profiles of isolated SIDM haloes with the simulations. We find that tidal effects of SIDM subhaloes can be described with a framework developed for the case of collision-less dark matter, but minor revisions are necessary to explain our SIDM simulation results. As long as the cross section is less than $\sim 10 \text{ cm}^2/\text{g}$ and a plausible range of subhalo density profiles at redshifts of ~ 2 is assumed for initial states, our simulations do not exhibit a prominent feature of gravothermal collapse in the subhalo central density for 10 Gyr. We develop a semi-analytic model of SIDM subhaloes in a time-evolving density core of the host with tidal stripping and self-scattering ram pressure effects. Our semi-analytic approach provides a simple, efficient and physically-intuitive prediction of SIDM subhaloes, but further improvements are needed to account for baryonic effects in the host and the gravothermal instability accelerated by tidal stripping effects.

Key words: Galaxies: structure – cosmology: dark matter

1 INTRODUCTION

An array of astronomical observations has established a concordance cosmological model, referred to as Λ Cold Dark Matter (Λ CDM) model. The Λ CDM model requires the presence of invisible mass components in the Universe to explain the current observational data. The nature of such “dark” matter is still uncertain. Because dark matter plays an essential role in formation and evolution of cosmic large-scale structures, the observations of large-scale structures have constrained the cosmic abundance of dark matter in the Universe (e.g. [Planck Collaboration et al. 2020](#); [Alam et al. 2021](#)), free-streaming effects induced by thermal motion of dark matter particles (e.g. [Baur et al. 2016](#); [Palanque-Delabrouille et al. 2020](#)), non-gravitational scattering of baryons and dark matter (e.g. [Dvorkin et al. 2014](#); [Xu et al. 2018](#)), electrically charged dark matter (e.g. [Kamada et al. 2017a](#)), and annihilation and decay processes of dark matter particles (e.g. [Ando & Ishiwata 2015](#); [Shirasaki et al. 2016](#); [Slatyer & Wu 2017](#); [Kawasaki et al. 2021](#)). So far, all constraints by the large-scale structures indicate that gravitational interactions are dominant in the growth of dark matter density, dark matter does not interact with ordinary matter and/or electromagnetic radiation, and its thermal motion is negligible.

Although the Λ CDM model has provided an excellent fit to the

observational data on length scales longer than ~ 10 Mpc, it remains unclear if the model can be compatible with observations at smaller scales (e.g. [Bullock & Boylan-Kolchin 2017](#), for a review). Self-interacting dark matter (SIDM) has been proposed as a solution for the small-scale challenges to the Λ CDM model (e.g. [Spergel & Steinhardt 2000](#)). Elastic self-interactions among dark matter particles can lead to formation of a cored density profile, that is preferred by observations of galaxies and galaxy clusters. After its proposal, numerical simulations have played a central role to improve our understanding of the structure formation in the presence of dark matter self-interactions, whereas particle physics models have been proposed to realise the SIDM preferred by some astronomical observations (e.g. [Tulin & Yu 2018](#), for a review).

Recently, [Oman et al. \(2015\)](#) found that rotation curves of observed spiral galaxies exhibit a diversity at their inner regions. This diversity problem appears to conflict with the Λ CDM prediction, but it can be explained within a SIDM framework (e.g. [Kamada et al. 2017b](#); [Ren et al. 2019](#); [Kaplinghat et al. 2020](#)). Nevertheless, it would be worth noting that the SIDM solution to the diversity problem depends on the sampling of halo concentration as well as co-evolution of dark matter with baryons (e.g. [Creasey et al. 2017](#); [Santos-Santos et al. 2020](#); [Sameie et al. 2021](#)).

Satellite galaxies in the Milky Way (denoted as MW satellites) are promising targets for robustly constraining the SIDM scenarios. The MW satellites are expected to be dominated by dark matter, and

* Contact e-mail: masato.shirasaki@nao.ac.jp

their dark matter contents would be less affected by possible baryonic effects inside the satellites. [Valli & Yu \(2018\)](#) examined the cross section of dark matter self-interactions with kinematic observations of MW dwarf spheroidals, but their modelling of SIDM density profiles does not include tidal effects from the host. A similar investigation has been done for less massive satellites known as ultra-faint dwarf galaxies in [Hayashi et al. \(2021\)](#). [Kaplinghat et al. \(2019\)](#) pointed out an anti-correlation between the central dark-matter densities of the bright MW satellites and their orbital peri-center distances inferred from Gaia data. The anti-correlation can be explained by a SIDM model (e.g. [Correa 2021](#)), while a more careful modelling of the kinematic observations leads that the Λ CDM predictions can explain the anti-correlation (e.g. [Hayashi et al. 2020](#))

High-resolution numerical simulations provide a powerful means of predicting the MW satellites in the presence of dark matter self-interactions (e.g. [Zavala et al. 2019](#); [Ebisu et al. 2022](#); [Silverman et al. 2022](#)) and the interplay with baryonic effects (e.g. [Robles et al. 2019](#); [Lovell et al. 2020](#); [Orkney et al. 2021](#)). However, numerical simulations can suffer from resolution effects and are commonly expensive to scan a wider range of parameters of interest. In practice, we need to account for various modelling uncertainties (e.g. possible baryonic effects and galaxy-halo connections) as well as several observational systematic effects to place a meaningful constraint of the nature of dark matter with the observations of the MW satellites (e.g. [Nadler et al. 2021](#); [Kim & Peter 2021](#)). Looking towards future measurements in wide-field spectroscopic surveys (e.g. [Takada et al. 2014](#)), an efficient semi-analytic modelling of the MW satellites in the presence of dark matter self-interactions is highly demanded.

In this paper, we aim at developing a semi-analytic model of the SIDM satellite haloes (denoted as subhaloes) in a MW-sized host halo. For this purpose, we perform a set of (dark-matter-only) N-body simulations of halo-subhalo mergers by varying the self-interacting cross sections, subhalo orbits, and internal properties of the subhaloes at their initial state. For comparisons, we formulate a simple semi-analytic model of the SIDM subhaloes accreting onto the host halo based on previous findings for the collision-less dark matter (e.g. [Green & van den Bosch 2019](#); [Jiang et al. 2021b](#)). We then calibrate our semi-analytic model with the idealised N-body simulations and assess its limitation. Our analysis would make an important first step toward a more precise modelling of the SIDM subhaloes, as well as improve our physical understanding of evolution of the SIDM subhaloes.

The rest of this paper is organised as follows. We describe our N-body simulations in Section 2. Next, we summarise our semi-analytic model of the SIDM subhaloes in Section 3. Section 4 presents the key results, whereas we discuss the limitations of our analysis in Section 5. Finally, concluding remarks are provided in Section 6. In the following, \ln represents the natural logarithm. Throughout this paper, we adopt Λ CDM cosmological parameters below; the average cosmic mass density $\Omega_m = 0.315$, the cosmological constant $\Omega_\Lambda = 1 - \Omega_m = 0.685$, the average baryon density $\Omega_b = 0.0497$, the present-day Hubble parameter $H_0 = 100h = 67.3 \text{ km/s/Mpc}$, the spectral index of the power spectrum of primordial curvature perturbations $n_s = 0.96$, and the linear mass variance within 8 Mpc/h being $\sigma_8 = 0.80$. Those parameters are consistent with statistical analyses of cosmic microwave backgrounds in [Planck Collaboration et al. \(2020\)](#). If necessary, we compute the critical density of the universe as $\rho_{\text{crit},z} = 2.775 \times 10^{11} [\Omega_m(1+z)^3 + \Omega_\Lambda] h^2 M_\odot/\text{Mpc}^3$, where z is a redshift.

2 SIMULATIONS

In this paper, we perform N-body simulations of idealised minor mergers to study evolution of single subhaloes in an external potential by a host halo for SIDM models. This section summarises how to set initial conditions of our N-body simulations, our N-body simulation code, and physical parameter sets adopted in our simulations.

2.1 Initial conditions

We assume that either host halo or subhalo at its initial state follows a spherical Navarro-Frenk-White (NFW; [Navarro et al. 1997](#)) density profile. At a given halo-centric radius r , the NFW profile is given by

$$\rho_{\text{NFW}}(r) = \frac{\rho_s}{(r/r_s)(1+r/r_s)^2}, \quad (1)$$

where ρ_s and r_s represent the scaled density and radius, respectively. The scaled density and radius can be related to a spherical over-density mass as

$$M_\Delta = \frac{4\pi}{3} \Delta \rho_{\text{crit},z} r_\Delta^3 = \int_0^{r_\Delta} 4\pi r^2 dr \rho_{\text{NFW}}(r), \quad (2)$$

where M_Δ is the spherical over-density mass and r_Δ is the corresponding halo radius. Throughout this paper, we adopt a conventional mass definition with $\Delta = 200$. The halo concentration is defined as $c = r_{200}/r_s$ and a set of c and M_{200} can fully determine the NFW profile. In the following, we use subscripts 'h' and 'sub' to indicate properties of the host- and sub-haloes, respectively.

For an initial condition of our N-body simulation, we fix the host halo mass, the halo radius and the scaled radius to $M_{200,h} = 10^{12} M_\odot$, $r_{200,h} = 211 \text{ kpc}$, and $r_{s,h} = 21.1 \text{ kpc}$, respectively. Note that the scaled density and radius of the host halo are set with the critical density at $z = 0$. For our fiducial case, we adopt $M_{200,\text{sub}} = 10^9 M_\odot$ and $c_{\text{sub}} = 6$ in the initial subhalo density, but we vary $M_{200,\text{sub}}$ and c_{sub} as necessary. The initial subhalo concentration is set to be consistent with a model prediction in [Diemer & Kravtsov \(2015\)](#) at $z = 2$. It would be worth noting that the redshift of $z = 2$ provides a typical formation epoch of the $\sim 10^{12} M_\odot$ halo at $z = 0$ in the excursion set approach ([Bond et al. 1991](#); [Lacey & Cole 1993](#)). To keep a consistency with our choice of $c_{\text{sub}} = 6$, we determine $\rho_{s,\text{sub}}$ and $r_{s,\text{sub}}$ with the critical density at $z = 2$. Using different redshifts to define the initial density profiles of the host and subhalo is a bit ambiguous, but our simulations do not contain accreting mass around the host and there are no unique ways to realise a realistic situation as in cosmological simulations. Because the outskirts region of the host halo is less important for orbital evolution of the subhalo, our simulations would be still useful to develop a better physical understanding of orbiting SIDM subhaloes.

To generate isolated NFW host halo and subhalo, we use a public code of MAGI ([Miki & Umemura 2018](#)), assuming that the NFW (sub)halo has an isotropic velocity distribution. The code employs a distribution-function-based method so that the phase-space distribution of member particles in halos can be determined by energy alone. To realise the system of particles in dynamical equilibrium with a sharp cut-off at $r \simeq r_{200}$, we multiply the target NFW density profile with a function of $\text{erfc}([r - r_{200}]/[2r_{\text{cut}}])/2$, where we adopt $r_{\text{cut}} = 0.05 r_{200}$. The number of particles is set to 10^7 for the host halo, corresponding to the particle mass being $m_{\text{part}} = 10^5 M_\odot$. The convergence tests of our N-body simulations are summarised in Appendix A. We confirmed that our choice of the particle mass can provide converged results of subhalo mass loss with a level of 1%, and subhalo density profiles at $r/r_{s,\text{sub}} \gtrsim 0.3$ within 10% over 10 Gyr.

To specify the subhalo orbit, we introduce two dimensionless quantities x_c and η . In this paper, we express the angular momentum L and the total energy E of the orbiting subhalo as

$$L = \eta r_c V_c \quad (3)$$

$$E = \frac{V_c^2}{2} + \Phi_{\text{NFW,h}}(r_c), \quad (4)$$

where $r_c = x_c r_{200,\text{h}}$, $V_c = (GM_{200,\text{h}}/r_c)^{1/2}$ is a velocity at the circular orbit when we treat host- and sub-halos as isolated point particles, and $\Phi_{\text{NFW,h}}$ presents the gravitational potential by the host NFW profile (Lokas & Mamon 2001). The orbital period T_r is then defined by

$$T_r = \int_{r_p}^{r_a} \frac{dr}{(2[E - \Phi_{\text{NFW,h}}(r)] - L^2/r^2)^{1/2}}, \quad (5)$$

where two radii r_p and r_a are given as a solution of the equation below:

$$\frac{L^2}{r^2} + 2[\Phi_{\text{NFW,h}}(r) - E] = 0. \quad (6)$$

The parameter x_c controls the orbital period, whereas η determines the eccentricity in the subhalo orbit. We choose $x_c = 0.5$ and $\eta = 0.6$ as our baseline parameters, while we examine different values to test our semi-analytic model described in Section 3. The baseline parameters provide $r_p = 41.9$ kpc, $r_a = 243$ kpc and $T_r = 3.0$ Gyr for our host halo. For a given set of x_c and η , we compute the initial (Cartesian) vectors of the subhalo position and velocity with respect to the host halo as $\mathbf{x}_{\text{sub}} = (r_a, 0, 0)$ and $\mathbf{v}_{\text{sub}} = (0, L/r_a, 0)$, respectively. Note that the subhalo orbit is confined to the $x-y$ plane in our simulations.

2.2 N-body simulations

For a given initial condition of halo mergers, we evolve the system by solving gravitational and self-interactions among N-body particles. To do so, we use a (non-cosmological) self-gravity mode of a flexible, massively-parallel, multi-method multi-physics code GIZMO (Hopkins 2015) for the gravitational interaction.

For the self-interaction scattering of N-body particles, we follow a standard Monte Carlo approach (e.g. Koda & Shapiro 2011; Vogelsberger et al. 2012). Throughout this paper, we assume isotropic and elastic self-interaction processes in our simulations. We calculate the dark matter density around the i -th dark matter particle in the same way as in the smoothed particle hydrodynamics (Lucy 1977; Gingold & Monaghan 1977):

$$\rho_i = \sum_j m_j W(r_{ij}, h_i), \quad (7)$$

where m_j is the mass of the j -th dark matter particle¹, r_{ij} is the distance between i -th and j -th particles, h_i is the smoothing length for the i -th particle, and $W(r_{ij}, h_i)$ is the cubic spline kernel function:

$$W(r, h) = \frac{8}{\pi h^3} \begin{cases} 1 + 6\left(\frac{r}{h}\right)^2 \left(\frac{r}{h} - 1\right) & \text{for } 0 \leq \frac{r}{h} < \frac{1}{2} \\ 2\left(1 - \frac{r}{h}\right)^3 & \text{for } \frac{1}{2} \leq \frac{r}{h} < 1 \\ 0 & \text{otherwise.} \end{cases} \quad (8)$$

¹ This is the mass of a numerical element and should be distinguished from the SIDM mass, m .

We determine the smoothing length so that the effective number of neighbours is some constant (Hopkins 2015) as

$$\frac{4\pi}{3} h_i^3 \sum_j W(r_{ij}, h_i) = N_{\text{ngb}}. \quad (9)$$

Throughout this paper, we employ $N_{\text{ngb}} = 32$.

The scattering rate between a particle i with its neighbour j is then given as

$$\mathcal{R}_{ij} = m_j W(r_{ij}, h_i) \frac{\sigma(v_{ij})}{m} v_{ij}, \quad (10)$$

where v_{ij} is the relative speed between particles i and j , and σ/m is the scattering cross-section per unit mass. The rate at which a particle i is scattered by any of its neighbours is therefore

$$\mathcal{R}_i = \sum_j m_j W(r_{ij}, h_i) \frac{\sigma(v_{ij})}{m} v_{ij}. \quad (11)$$

To simplify the implementation for the parallel computation, we represent the scattering between the particle i and its neighbours as the scattering between the particle i and its nearest neighbour. Namely, the collision between the particle i and its nearest neighbour during a time-step Δt_i takes place with the probability:

$$p_i = \frac{\mathcal{R}_i}{2} \Delta t_i. \quad (12)$$

We introduce the factor 1/2 since a scatter event always involves a pair of particles. To avoid multiple scattering during a time-step, we restrict the time-step Δt_i to be smaller than $0.02/\mathcal{R}_i$.

The box size on a side is set to 1100 kpc so that the boundary of our simulation box can not affect the simulation results. We also adopt the gravitational softening length, in terms of an equivalent-Plummer value, ϵ , as proposed in van den Bosch & Ogiya (2018);

$$\epsilon = 0.05 r_{s,\text{sub}} \left(\frac{N_{\text{sub}}}{10^5} \right)^{-1/3}, \quad (13)$$

where N_{sub} represents the number of N-body member particles in initial subhaloes and is set to $N_{\text{sub}} = 10^4$ for our baseline run. All simulations output particle snapshots with a fixed time-step of 0.1 Gyr and stop at $t = 10$ Gyr. At each snapshot, we define gravitational-bound particles in the subhalo with the iterative method in van den Bosch & Ogiya (2018).

2.3 Parameters

Table 1 summarises a set of parameters adopted in our N-body simulations. Most simulations assume that the SIDM cross section per unit mass σ/m is independent of relative velocities between dark matter particles, but we also explore the impact of a velocity-dependent σ/m by adopting effective-range theories in Chu et al. (2020). To be specific, we adopt a velocity-dependent scenario as in Chu et al. (2020);

$$\frac{\sigma}{m} = \frac{\sigma_0}{m} \left\{ \left[1 - \frac{1}{8} \frac{r_e}{a} \left(\frac{v}{v_0} \right)^2 \right]^2 + \frac{1}{4} \left(\frac{v}{v_0} \right)^2 \right\}^{-1}, \quad (14)$$

where we set $\sigma_0/m = 6.3 \text{ cm}^2/\text{g}$, $a = 37.4 \text{ fm}$, $r_e = -748.9 \text{ fm}$, and $v_0 = 100 \text{ km/s}$ and those parameters provide a reasonable fit to the observational constraints of $\langle \sigma v \rangle / m$ at the average relative velocity of $\langle v \rangle = 10 - 100 \text{ km/s}$ in Kaplinghat et al. (2016). This velocity-dependent model predicts that an effective cross section $\langle \sigma v \rangle / m / \langle v \rangle$ is found to be $1 - 6 \text{ cm}^2/\text{g}$ at the mass scale of $\sim 10^9 M_\odot$, while the

Table 1. Summary of parameters in our N-body simulations of halo mergers. For all simulations in this paper, we fix the host halo mass $M_{200,h} = 10^{12} M_{\odot}$, the scaled radius (in the initial NFW density) $r_{s,h} = 21.1$ kpc, and the concentration $c_h = 10$. In every simulation, we evolve the orbit of an infalling subhalo for 10 Gyr. Note that our simulations allow a time evolution of the host halo density in accord with the thermalisation due to the self-scattering process of dark matter particles. In each cell, $M_{200,sub}$ is the initial subhalo mass, $r_{s,sub}$ is the scaled radius in the initial subhalo density, c_{sub} is the subhalo concentration at its initial state, σ/m is the self-scattering cross section per unit mass, and (x_c, η) present dimensionless orbital parameters described in Subsection 2.1.

Name	$M_{200,sub} (M_{\odot})$	$r_{s,sub} (\text{kpc})$	c_{sub}	$\sigma/m (\text{cm}^2/\text{g})$	(x_c, η)
Fiducial (v -independent σ/m)					
CDM	10^9	1.68	6	0	(0.5, 0.6)
SIDM1	10^9	1.68	6	1	(0.5, 0.6)
SIDM3	10^9	1.68	6	3	(0.5, 0.6)
SIDM10	10^9	1.68	6	10	(0.5, 0.6)
v -dependent σ/m					
vSIDM	10^9	1.68	6	Eq. (14)	(0.5, 0.6)
Different orbits					
SIDM1-diff-orbit	10^9	1.68	6	1	(0.6, 0.05), (0.6, 0.35), (0.6, 0.65), (0.6, 0.95) (0.9, 0.05), (0.9, 0.35), (0.9, 0.65), (0.9, 0.95) (1.2, 0.05), (1.2, 0.35), (1.2, 0.65), (1.2, 0.95) (1.5, 0.05), (1.5, 0.35), (1.5, 0.65), (1.5, 0.95)
Varied subhalo properties					
High c_{sub}	10^9	0.842	12	1	(0.5, 0.6)
Low c_{sub}	10^9	3.36	3	1	(0.5, 0.6)
Large M_{sub}	10^{10}	4.38	5	1	(0.5, 0.6)

cross section becomes smaller than $\sim 0.1 \text{ cm}^2/\text{g}$ for a MW-sized halo.

Apart from our fiducial orbital parameters ($x_c = 0.5$ and $\eta = 0.6$), we also examine 16 different orbits in a range of $0.6 \leq x_c \leq 1.5$ and $0.05 \leq \eta \leq 0.95$. Note that the range of x_c and η is consistent with the cosmological N-body simulation in Jiang et al. (2015). For the initial density profile of an infalling subhalo, we vary the halo concentration by a factor of 2 or 1/2 but fix subhalo mass to $M_{200,sub} = 10^9 M_{\odot}$. The change of c_{sub} by a factor of 2 or 1/2 roughly covers a 2.5σ -level difference in the halo concentration at the mass of $10^9 M_{\odot}$ in cosmological simulations (e.g. Ishiyama et al. 2013). As another test, we consider a more massive infalling subhalo with $M_{200,sub} = 10^{10} M_{\odot}$ and $c_{sub} = 5$. As in Subsection 2.1, the density profile for the $10^{10} M_{\odot}$ subhalo is set with the critical density at $z = 2$.

3 MODEL

This section describes our semi-analytic model of orbital and dynamical evolution of an infalling subhalo in the presence of self-interactions of dark matter particles. The model consists of three ingredients; (i) a time-evolving SIDM density profile in isolation (Subsection 3.1), (ii) the equation of motion of the subhalo including dynamical friction and ram-pressure-induced deceleration (Subsection 3.2), and (iii) mass loss of the subhalo across its orbit (Subsection 3.3). In the Subsections 3.1-3.3, we first assume a velocity-independent cross section σ/m for simplicity. We then describe how to include the velocity-dependence of σ/m in our model in Subsection 3.4.

3.1 Gravothermal fluid model

In our model, we follow a gravothermal fluid model (e.g. Balberg et al. 2002) to predict spherical density profiles of isolated haloes. The gravothermal fluid model assumes that SIDM consists of a thermally conducting fluid in quasistatic equilibrium and the system of interest is isotropic and spherically-symmetric. At a given time of t and halo-centric radius of r , dark matter particles have a mass density profile $\rho(r, t)$. Their one-dimensional (1D) velocity dispersion $\sigma_v(r, t)$ is set by the hydrostatic equilibrium of ideal gas at each moment;

$$\frac{\partial p(r, t)}{\partial r} = -\frac{GM(r, t)\rho(r, t)}{r^2}, \quad (15)$$

where $p = \rho \sigma_v^2$ is an effective pressure, $M(r, t)$ is the enclosed mass within the radius of r at t , and we impose the mass conservation of

$$\frac{\partial M(r, t)}{\partial r} = 4\pi r^2 \rho(r, t). \quad (16)$$

The thermal evolution of the fluid is governed by Fourier's law of thermal conduction and the first law of thermodynamics,

$$\begin{aligned} \frac{L(r, t)}{4\pi r^2} &= -\kappa \frac{\partial T(r, t)}{\partial r}, \\ \frac{\partial L(r, t)}{\partial r} &= -4\pi r^2 p(r, t) \left(\frac{\partial}{\partial t} \right)_M \ln \left(\frac{\sigma_v^3(r, t)}{\rho(r, t)} \right), \end{aligned} \quad (17)$$

where $L(r, t)$ is the luminosity through a sphere at r , $T(r, t)$ is a temperature defined as $k_B T = m \sigma_v^2$ (m is the particle mass and k_B is the Boltzmann constant), κ is the thermal conductivity, and the time derivative in the right hand side of Eq. (18) is Lagrangian.

As discussed in Balberg et al. (2002), we adopt a single expression of Eq. (17) by considering both the cases where the mean free path between collisions is significantly shorter or larger than the system

size,

$$\frac{L}{4\pi r^2} = -\frac{3}{2}b_*\rho\sigma_v \left[\left(\frac{1}{\lambda} \right) + \left(\frac{b_*\sigma_v t_r}{C_* H_g^2} \right) \right]^{-1} \frac{\partial \sigma_v^2}{\partial r}, \quad (19)$$

where $H_g \equiv \sqrt{\sigma_v^2/(4\pi G\rho)}$ is the gravitational scale height of the system, $\lambda = (\rho\sigma/m)^{-1}$ is the collisional scale for the mean free path, $t_r \equiv \lambda/(a\sigma_v)$ is the relaxation time with a coefficient of order of unity being a , and we adopt $a = \sqrt{16/\pi}$ for hard-sphere scattering of particles with a Maxwell-Boltzmann velocity distribution (Reif 1965).

In Eq. (19), we introduce two model parameters of b_* and C_* . In the limit of $\lambda \ll H_g$, the thermal conductivity is given by $\kappa \simeq (3/2)(k_B/m)b_*\rho\lambda^2/(at_r)$ and b_* can be regarded as an effective impact parameter among particle collisions. In the limit of $\lambda \gg H_g$, one finds $\kappa \simeq (3/2)(k_B/m)C_*\rho H_g^2/t_r$, reproducing an empirical formula of gravothermal collapse of globular clusters (Lynden-Bell & Eggleton 1980). As our baseline model, we adopt $b_* = 0.25$ and $C_* = 0.75$ as proposed in Koda & Shapiro (2011). By assuming the NFW halo at $t = 0$, we then numerically solve Eqs. (15), (16), (18) and (19) with the method described in Appendix A of Nishikawa et al. (2020) (also see Pollack et al. 2015).

We note that Koda & Shapiro (2011) found the parameters of $b_* = 0.25$ and $C_* = 0.75$ to explain their N-body simulations of isolated haloes following a self-similar solution of the gravothermal fluid model in Balberg et al. (2002). Hence, we validate the gravothermal fluid model with $b_* = 0.25$ and $C_* = 0.75$ for NFW haloes at $t = 0$ by using our N-body simulations of isolated haloes. The comparisons with the gravothermal fluid model and our simulation results are summarised in Appendix B. We find that a correction of the gravothermal fluid model is needed to explain our simulation results for initial NFW haloes with their mass of $M_{200} = 10^{12} M_\odot$ and concentration of $c = 10$ in the range of $0.3 \lesssim \sigma/m$ (cm^2/g) $\lesssim 30$ at $t \leq 10$ Gyr. The final model of density profiles of isolated SIDM haloes is then given by

$$\rho_{\text{SIDM}}(r, t) = \rho_{\text{gt}}(r, t) \frac{N(x^\beta + \alpha^\beta)}{(x + \gamma)^\beta}, \quad (20)$$

where $\rho_{\text{gt}}(r, t)$ is the gravothermal-fluid prediction with $b_* = 0.25$ and $C_* = 0.75$ and $x = r/r_s$ (r_s is the scaled radius of the initial NFW halo). The four parameters N , α , β and γ in Eq. (20) depend on time as well as σ/m ;

$$N = \begin{cases} 1 & t/t_0 < 2 \\ 1 + 0.060(t/t_0 - 2)^{0.444} & t/t_0 \geq 2 \end{cases}, \quad (21)$$

$$\alpha = 0.865(t/t_0)^{0.436}(t/t_0 + 48.3)^{-0.71}, \quad (22)$$

$$\beta = 2.10(t/t_0)^{0.0723}, \quad (23)$$

$$\gamma = 3.54(t/t_0)^{0.880}(t/t_0 + 74.3)^{-1.08}, \quad (24)$$

where we introduce a characteristic time scale of

$$\begin{aligned} t_0 &\equiv \left(\sqrt{\frac{16}{\pi}} \rho_s \frac{\sigma}{m} \sqrt{4\pi G \rho_s r_s^2} \right)^{-1} \\ &= 1.29 \text{ Gyr} \left(\frac{\sigma/m}{1 \text{ cm}^2/\text{g}} \right)^{-1} \left(\frac{\rho_s}{5 \times 10^6 M_\odot \text{ kpc}^{-3}} \right)^{-3/2} \left(\frac{r_s}{20 \text{ kpc}} \right)^{-1} \end{aligned} \quad (25)$$

and note that $\sqrt{4\pi G \rho_s r_s^2}$ in the above equation provides a characteristic velocity for the initial NFW haloes. Our model has been calibrated with N-body simulations of isolated SIDM haloes with the specific initial NFW profile ($M_{200} = 10^{12} M_\odot$, $r_{200} = 211$ kpc, $r_s = 21.1$ kpc and $\rho_s = 5.72 \times 10^6 M_\odot \text{ kpc}^{-3}$), but we use Eq. (20) for any initial NFW profiles in the following.

3.2 Orbital evolution

Assuming that the subhalo is not significantly deformed by tidal forces and self-interactions, we treat it as a point particle. Under this point-mass approximation, we evaluate the orbit of the subhalo by solving the equation of motion (e.g. Jiang et al. 2021a,b, for the same approach),

$$\frac{d^2 \mathbf{x}_{\text{sub}}}{dt^2} = -\nabla \Phi_{\text{h}} + \mathbf{a}_{\text{DF}} + \mathbf{a}_{\text{RPd}}, \quad (26)$$

where Φ_{h} is the gravitational potential of a SIDM host halo with its density following Eq. (20), \mathbf{a}_{DF} represents the acceleration due to dynamical friction, and \mathbf{a}_{RPd} is the deceleration causing by the scattering process among escaping dark matter particles from the infalling subhalo and particles in the host halo (Kummer et al. 2018).

On the term of dynamical friction, we adopt the Chandrasekhar formula (Chandrasekhar 1943) as

$$\mathbf{a}_{\text{DF}} = -4\pi G^2 M_{\text{sub}} \rho_{\text{h}} \ln \Lambda F_V(|\mathbf{v}_{\text{sub}}|) \frac{\mathbf{v}_{\text{sub}}}{|\mathbf{v}_{\text{sub}}|^3}, \quad (27)$$

where we adopt an expression of the Coulomb logarithm as $\ln \Lambda = \xi \ln(M_{\text{h}}/M_{\text{sub}})$ with a fudge factor of ξ being $\min(|\ln \rho_{\text{h}}/d \ln r|, 1)$ at $r = |\mathbf{x}_{\text{sub}}|$ as proposed in Read et al. (2006), and

$$F_V(v) = \text{Erf}(y) - 2y \exp(-y^2)/\sqrt{\pi} \quad (28)$$

with $y = v/(\sqrt{2}\sigma_{v,\text{h}})$ for an isotropic and Maxwellian host halo. The velocity dispersion of $\sigma_{v,\text{h}}$ is given by the solution of Eq. (15) with the density profile of ρ_{h} .

The scattering-induced deceleration term is given by

$$\mathbf{a}_{\text{RPd}} = -\mathbf{v}_{\text{sub}} \eta_{\text{d}} \left(\frac{\sigma |\mathbf{v}_{\text{sub}}|}{m} \right) \rho_{\text{h}}, \quad (29)$$

where η_{d} is the deceleration fraction computed as (see Markevitch et al. 2004; Kummer et al. 2018)

$$\eta_{\text{d}} = 1 - 4 \int_{x/\sqrt{(1+x)^2}}^1 dy y^2 \sqrt{y^2 - x^2(1-y^2)}, \quad (30)$$

$$x = \frac{\bar{v}_{\text{esc,sub}}}{\sqrt{|\mathbf{v}_{\text{sub}}|^2 + \sigma_{v,\text{h}}^2}}, \quad (31)$$

$$\bar{v}_{\text{esc,sub}} = \frac{1}{M_{\text{sub}}} \int 4\pi r^2 dr \rho_{\text{sub}} \sqrt{-2\Phi_{\text{sub}}}. \quad (32)$$

In the above, Φ_{sub} is the gravitational potential of the subhalo. Note that we account for the bulk velocity of the subhalo as well as the random velocity of the particles inside the host halo in the computation of η_{d} (see Appendix A in Kummer et al. 2018, for details). Nevertheless, the effect of \mathbf{a}_{RPd} is found to be almost negligible for our simulation results in this paper.

We solve Eq. (26) using a fourth-order Runge-Kutta method. It would be worth noting that we properly include the time evolution of the host halo density ρ_{h} across the subhalo orbit as in Subsection 3.1. To solve Eq. (26), we require a model of mass loss of the subhalo as well as the change of the subhalo density profile ρ_{sub} due to tidal effects and ram-pressure evaporation, described in the next Subsection.

3.3 Mass loss

In the SIDM model, the infalling subhalo can lose its mass due to tidal stripping and ram-pressure evaporation effects. The former effect can predominantly remove mass from the outskirts of the subhalo, while

the latter can affect the mass density in the entire region of the subhalo.

For the tidal stripping, we employ a commonly-used expression of the mass loss rate, given by

$$\left(\frac{dM_{\text{sub}}}{dt}\right)_{\text{TS}} = -\mathcal{A} \frac{M_{\text{sub}}(> r_t; t)}{q\tau_{\text{dyn}}(R)}, \quad (33)$$

where \mathcal{A} is a free parameter in the model, $M_{\text{sub}}(> r_t; t)$ represents the subhalo mass in the outskirts with $r > r_t$ at t , $\tau_{\text{dyn}}(R)$ is the dynamical time at the relative distance between the subhalo and the host centre being R , and q is a parameter with an order of unity. To be specific, we define the dynamical time as

$$\tau_{\text{dyn}}(R) = \sqrt{\frac{\pi^2 R^3}{4GM_{\text{h}}(R)}}, \quad (34)$$

and note that $M_{\text{h}}(R)$ is the enclosed mass of the host and depends on time t . We account for possible effects of (sub)halo concentrations at initial states by setting $q = (c_{\text{sub}}/c_{\text{h}}/2)^{1/3}$ (motivated by the results in [Green et al. 2021](#)). The value of \mathcal{A} will be calibrated with our simulations. The radius of r_t is known as the tidal radius, and there are a number of different definitions (e.g. see [van den Bosch et al. 2018](#), for a brief overview). In this paper, we adopt a phenomenological model of

$$r_t = \min(r_{t1}, r_{t2}), \quad (35)$$

with

$$\frac{r_{t1}}{R} = \left[\frac{M_{\text{sub}}(r_{t1})/M_{\text{h}}(R)}{2 - (d \ln M_{\text{h}}/d \ln r)_{r=R} + (v_{\text{tan,sub}}/v_{\text{circ,h}}(R))^2} \right]^{1/3} \quad (36)$$

$$\frac{r_{t2}}{R} = \left(\frac{M_{\text{sub}}(r_{t2})}{M_{\text{h}}(R)} \right)^{1/3}, \quad (37)$$

where $v_{\text{tan,sub}} = |\mathbf{x}_{\text{sub}} \times \mathbf{v}_{\text{sub}}|/|\mathbf{x}_{\text{sub}}|$ is the instantaneous tangential velocity of the subhalo, and $v_{\text{circ,h}}(R) = \sqrt{GM_{\text{h}}(R)/R^2}$ represents the circular velocity of a test particle in the host at the radius of R . Note that one derives Eq. (36) by assuming that the subhalo can be approximated as a point mass on a circular orbit ([von Hoerner 1957](#); [King 1962](#)), while the assumption becomes invalid for more radial orbits. Eq. (37) has been proposed in [Klypin et al. \(1999\)](#) to account for resonances between the gravitational force by the subhalo and the tidal force by the host ([Weinberg 1994a,b, 1997](#)). If we can not find a non-trivial solution of $r_{t1} \neq 0$ in Eq. (36), we set $r_t = r_{t2}$.

For the ram-pressure evaporation, we adopt the mass loss rate below ([Kummer et al. 2018](#))

$$\left(\frac{dM_{\text{sub}}}{dt}\right)_{\text{RPe}} = -M_{\text{sub}} \eta_e \left(\frac{\sigma |\mathbf{v}_{\text{sub}}|}{m} \right) \rho_{\text{h}}, \quad (38)$$

where η_e is the evaporation fraction computed as (see [Markevitch et al. 2004](#); [Kummer et al. 2018](#))

$$\eta_e = \frac{1 - x^2}{1 + x^2}, \quad (39)$$

and x in the above is given by Eq. (31).

At each moment t , we can compute the mass loss of the subhalo during a small time interval of Δt by using Eqs. (33) and (38). We then reset the subhalo mass of

$$M_{\text{sub}} \rightarrow M_{\text{sub}} + \Delta t \left(\frac{dM_{\text{sub}}}{dt}\right)_{\text{TS}} + \Delta t \left(\frac{dM_{\text{sub}}}{dt}\right)_{\text{RPe}}, \quad (40)$$

and include effective tidal stripping effects on the subhalo density profile as

$$\rho_{\text{sub}}(r, t + \Delta t) = \rho_{\text{SIDM,sub}}(r, t + \Delta t) H(r; f_{\text{b}}, c_{\text{sub}}), \quad (41)$$

where $\rho_{\text{SIDM,sub}}(r, t)$ is the model of Eq. (20) for the subhalo, f_{b} is the bound mass defined as $M_{\text{sub}}(t + \Delta t)/M_{\text{sub}}(t = 0)$, and $H(r; f_{\text{b}}, c_{\text{sub}})$ presents the change of the subhalo density profile due to the tidal stripping (referred to as the transfer function in the literature). After updating the subhalo mass and its density profile, we then solve Eq. (26) to obtain the position and velocity of the subhalo at the time of $t + \Delta t$. In practice, we set the time-step Δt to be $10^{-4}T_r$ throughout this paper.

In Eq. (41), we assume that the ram-pressure effects are less important for the shape in the subhalo density profile, but the tidal stripping plays a central role. Tidal evolution of density profiles of infalling subhaloes has been investigated in [Ogiya et al. \(2019\)](#); [Green & van den Bosch \(2019\)](#) with a large set of N-body simulations of minor mergers for collision-less dark matter (i.e. $\sigma/m = 0$). [Green & van den Bosch \(2019\)](#) has studied the tidal evolution of the subhalo density profile with respect to its initial counterpart and found that the structural evolution of a tidally truncated subhalo is predominantly determined by the bound mass fraction f_{b} and the initial subhalo concentration. We here adopt their calibrated model of the transfer function H in Eq. (41). The explicit form of H is provided in Appendix C. It should be noted that [Green & van den Bosch \(2019\)](#) calibrated the form of H with the tidally stripped profile relative to the initial profile, but our model uses their transfer function for the time-evolving SIDM density profile. Although our model can reproduce the results in [Green & van den Bosch \(2019\)](#) in the limit of $\sigma/m \rightarrow 0$ and $\rho_{\text{SIDM,sub}} \rightarrow \rho_{\text{NFW,sub}}$, Eq. (41) should be validated with our N-body simulations for SIDM models. We summarise our validation of Eq. (41) in Subsection 4.1.

3.4 For velocity-dependent cross sections

We here explain how our model can be applied for velocity-dependent cross sections $\sigma(v)/m$. Suppose that we solve the time evolution of the system with an time interval of Δt . At the n -th time-step $t = t_n$, our model follows procedures below;

(i) We first determine the time evolution of density profiles for isolated host- and sub-haloes as in Subsection 3.1. For this purpose, we set effective cross sections to

$$\left(\frac{\sigma}{m}\right)_{\text{eff}} \equiv \frac{\langle \sigma v/m \rangle}{\langle v \rangle}, \quad (42)$$

$$\langle \sigma v/m \rangle = \int_0^{\infty} dv v \sigma(v)/m f(v; v_c), \quad (43)$$

$$\langle v \rangle = \int_0^{\infty} dv v f(v; v_c), \quad (44)$$

where $f(v; v_c)$ represents the distribution function of relative velocity of particles in the host or subhalo, and v_c determines a typical velocity scale. We define Eq. (42) with a velocity-weighted quantity because the number of particles scattered per unit time ($\propto \langle \sigma v/m \rangle$) is expected to be relevant to the evolution of SIDM density profiles. In this paper, we assume $f(v; v_c)$ as a Maxwell-Boltzmann distribution for relative velocities;

$$f(v; v_c) = \frac{4v_c^2 \exp(-v^2/v_c^2)}{\sqrt{\pi}v_c^3}, \quad (45)$$

providing that $\langle v \rangle = v_c$. For a given halo/subhalo density profile at $t = t_{n-1}$, we determine the 1D velocity dispersion $\sigma_v(r)$ by Eq. (15) and set $v_c = 4\sigma_v(r_s)/\sqrt{\pi}$ where r_s is the scaled radius at the initial NFW profile. We then take the corresponding SIDM density profile at $\sigma/m = (\sigma/m)_{\text{eff}}$ and the moment of $t = t_n$ from a pre-stored table of ρ_{SIDM} given by Eq. (20) for v -independent cross sections.

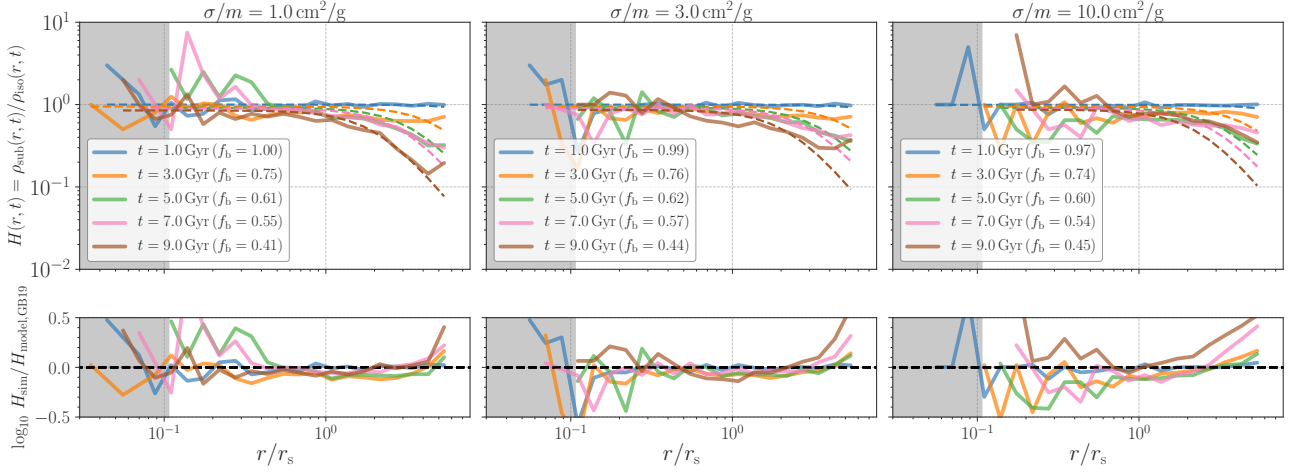


Figure 1. Structural evolution of density profiles of infalling subhaloes in SIDM models. From left to right, we show the results with the self-interacting cross section of $\sigma/m = 1, 3$ and $10 \text{ cm}^2/\text{g}$, respectively. For each model, the upper panel shows the transfer function of the subhalo density profile (denoted as $H(r, t)$) measured in our N-body simulations. Different coloured lines represent the results at different epochs ($t = 1, 3, 5, 7,$ and 9 Gyr). The dashed lines in the upper panels are model predictions in [Green & van den Bosch \(2019\)](#). The lower panels summarises the fractional difference between the simulation results and the model predictions. Note that numerical resolution effects would be important in the grey region in the figure. Although the model in [Green & van den Bosch \(2019\)](#) has been calibrated with N-body simulations with $\sigma/m = 0 \text{ cm}^2/\text{g}$, it can provide a reasonable fit to the simulation results with $1 \leq \sigma/m (\text{cm}^2/\text{g}) \leq 10$ if the mass fraction of subhalo bound mass f_b is set to the values in our N-body simulations. These results highlight that scattering processes between host- and sub-haloes are less important to determine the shape of the subhalo density profile, as long as we consider the cross section of $\sigma/m \lesssim 10 \text{ cm}^2/\text{g}$. Note that the host halo evolved and formed a cored density at its central region in our SIDM simulation. Hence, the mass loss rate of SIDM subhaloes with a larger σ/m can become smaller.

(ii) We then solve the equation of motion of the subhalo as in Subsection 3.2. To determine the ram-pressure deceleration term of Eq. (29), we substitute σ/m for $\sigma(|\mathbf{v}_{\text{sub},n-1}|)/m$, where $\mathbf{v}_{\text{sub},n-1}$ is the bulk velocity of the subhalo at $t = t_{n-1}$. Using the time-step of Δt , we also set the mass loss of the infalling subhalo and update the shape of the subhalo density profile as in Eq. (41). For the velocity-dependent cross section, we compute the mass loss of Eq. (38) by setting $\sigma/m = \sigma(|\mathbf{v}_{\text{sub},n-1}|)/m$.

(iii) After updating the bound mass, position, velocity, and the density profile of the subhalo, we go back to the step (i) to determine the density profiles at $t = t_{n+1}$.

4 RESULTS

This section presents main results in our paper. Those include the structural evolution of subhalo density profiles with dark matter self-interactions, detailed comparisons with our semi-analytic model and the simulation outputs, and discussion on differences between our model and others in the literature.

4.1 Structural evolution of SIDM subhaloes

We first study density profiles of infalling SIDM subhaloes at different epochs. As the subhalo orbit is evolved, the density profile is modified by gravitational interactions as well as the self-interaction of dark matter particles in the host and subhalo.

For ease of comparison, we run N-body simulations of an isolated halo with its initial mass of $10^9 M_\odot$ and concentration of 6, but varying $\sigma/m = 1, 3,$ and $10 \text{ cm}^2/\text{g}$. These isolated haloes are evolved by 10 Gyr with a snapshot interval of 0.1 Gyr. We then characterise

the structural evolution of infalling subhalo density profiles as

$$H(r, t) \equiv \frac{\rho_{\text{sub}}(r, t)}{\rho_{\text{iso}}(r, t)}, \quad (46)$$

where $\rho_{\text{sub}}(r, t)$ is the density profile of infalling subhaloes, and $\rho_{\text{iso}}(r, t)$ represents the counterpart for isolated haloes with the same initial density profiles as the subhaloes.

Figure 1 summarises our measurements of $H(r, t)$. At each column, upper and lower panels present the results at $\sigma/m = 1, 3$ and $10 \text{ cm}^2/\text{g}$ from left to right. Solid lines in the upper panel show the function of $H(r, t)$ in our simulations and the colour difference indicates the difference in the epoch t . The coloured dashed lines in the upper panel are the prediction in [Green & van den Bosch \(2019\)](#) with the simulated value of the bound mass fraction f_b . The fractional difference between the simulation results and the model prediction is shown in the lower panels.

We find that the structural evolution of SIDM subhaloes can be approximated as the model in [Green & van den Bosch \(2019\)](#), even though the model has been calibrated with the collision-less N-body simulations. As long as the cross section is set to smaller than $\sim 10 \text{ cm}^2/\text{g}$, the ram-pressure evaporation is less important to set the shape of the subhalo density profile. We here note that a reasonable match between the simulation results and the model in [Green & van den Bosch \(2019\)](#) occurs only when we use the value of f_b in the simulations. This highlights that a precise model of the mass loss is important to determine the density profile of the subhalo at outskirts across its orbit. Also, the results in Figure 1 support that our approximation of Eq. (41) would be valid if we can predict the density profile of SIDM halos in isolation. More detailed comparisons with the simulation results and Eq. (41) are presented in the next Subsection.

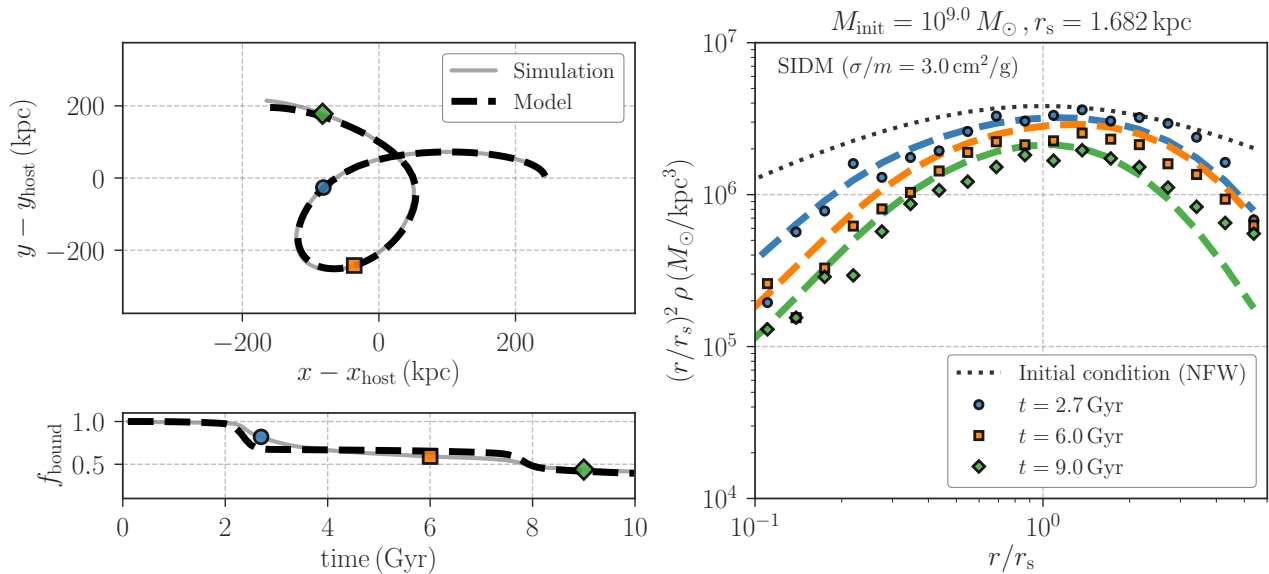


Figure 2. Comparisons with N-body simulation results and our semi-analytic model of infalling subhaloes. In this figure, we assume a velocity-independent cross section of $\sigma/m = 3 \text{ cm}^2/\text{g}$. The top left panel shows the orbital evolution of the subhalo over 10 Gyr, while the bottom left presents the mass evolution. The right panel summarises the time evolution of the subhalo density profile. In the right, blue circles, orange squares, and green diamonds represent the simulation results at $t = 2.7, 6.0,$ and 9.0 Gyr, respectively. In each panel, dashed lines are the model predictions.

4.2 Comparison with simulation results and model predictions

We here summarise comparisons with our N-body simulation results and model predictions as in Section 3.

4.2.1 Varying cross sections

We first investigate the dynamical evolution of infalling subhaloes with their initial mass of $10^9 M_\odot$ and a fixed subhalo orbital parameter as a function of the self-interaction cross section σ/m . For this purpose, we use the fiducial simulation runs of CDM, SIDM1, and SIDM3, and SIDM10 in Table 1.

Figure 2 summarises the simulation outputs of the infalling subhalo for the SIDM3 run ($\sigma/m = 3 \text{ cm}^2/\text{g}$) as well as our model predictions. In the left panels, grey lines represent the simulation results, while the dashed lines are our model predictions. For this figure, we set a parameter for the mass loss (see Eq. 33) to $\mathcal{A} = 0.45$. Our model provides an accurate fit to the subhalo orbit in our simulation over 10 Gyr, and the overall evolution of the subhalo mass can be captured by the simple model in Subsection 3.3. In the right panel, we compare the subhalo density profile at different epochs. The simulation results are shown by coloured symbols, and the dashed lines show the model predictions. The figure demonstrates that the structural evolution of the subhalo density profile can be explained by our phenomenological model of Eq. (41). The time evolution at $r \lesssim r_s$ can be well determined by the gravothermal fluid model with a correction (see Eq. 20), while the density at outskirts ($r \gtrsim r_s$) is suppressed mostly by tidal stripping processes.

Figure 3 shows how the dynamical evolution of the subhalo can depend on the cross section σ/m . The orbital evolution of the subhalo with different σ/m are summarised in the left, while the right shows the evolution of the subhalo mass over 10 Gyr. In each panel, solid lines represent our model predictions, providing a reasonable fit to the simulation results for various cross sections. We find that the model works when the parameter \mathcal{A} is set to 0.55, 0.50, 0.45 and 0.40

for the simulations with $\sigma/m = 0, 1, 3,$ and $10 \text{ cm}^2/\text{g}$, respectively. This marginal σ/m -dependence of the model parameter \mathcal{A} can be important in practice, especially when one would constrain the SIDM by using observations of MW satellites. We also note that the subhalo mass is more suppressed as σ/m becomes smaller in our simulations and this looks incompatible with recent studies (e.g. Sameie et al. 2020). The difference mainly arises from the time evolution of the host halo. In our simulations, the density of the host halo evolves and forms a core at the host centre due to the thermalisation. On the other hand, some previous studies assumed that the host halo is static and follows a cuspy NFW profile. These differences in the host halo can affect the dynamical evolution of infalling subhaloes, because the mass loss of subhaloes should depend on the host halo density (e.g. Peñarrubia et al. 2010).

We then examine the velocity-dependent model of σ/m as in Eq. (14) by using the vSIDM run (see Table 1). Figure 4 summarises the comparison of the simulation results with our semi-analytic model. Note that we set $\mathcal{A} = 0.40$ in Figure 4. The figure highlights that our treatment in Subsection 3.4 can explain the simulation results with an appropriate choice of \mathcal{A} . It would be worth noting that we observe more rapid loss of the subhalo mass in the vSIDM than the CDM. Because the model of Eq. (14) provides a small σ/m for the host halo, the host halo density is well approximated as a static NFW profile over 10 Gyr in the vSIDM run. Hence, the mass loss by self-scattering processes (Eq. 38) can give additional effects in the vSIDM compared to the CDM, leaving smaller bound mass of the subhalo in the vSIDM run.

4.2.2 Varying subhalo orbits

We next study the impact of subhalo orbits on the subhalo mass loss in SIDM models. We examine 16 different sets of our orbital parameters (x_c, η) as in Table 1 assuming the velocity-independent cross section of $\sigma/m = 1 \text{ cm}^2/\text{g}$.

Figure 5 summarises the time evolution of infalling subhalo masses

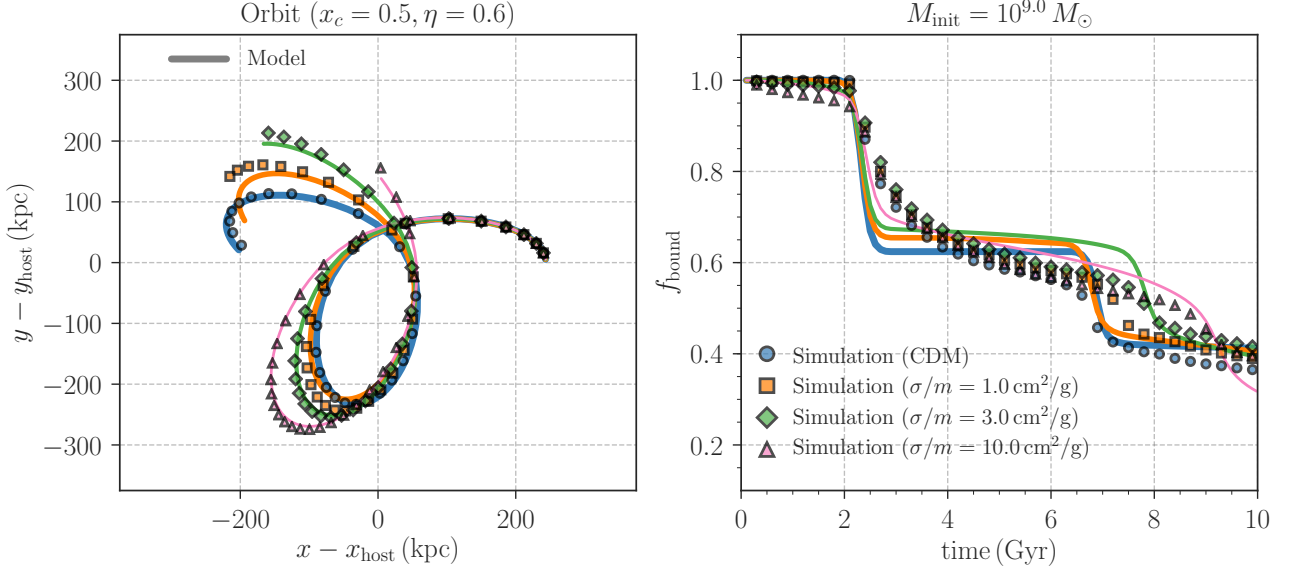


Figure 3. The orbital and mass evolution of an infalling subhalo with its initial mass of $10^9 M_{\odot}$ as a function of σ/m . In this figure, σ/m is assumed to be velocity-independent. In each panel, the blue circles, orange squares, green diamonds, and pink triangles represent the simulation results at $\sigma/m = 0, 1, 3,$ and $10 \text{ cm}^2/\text{g}$, respectively. Our model predictions are shown by different lines, providing a reasonable fit to the simulation results.

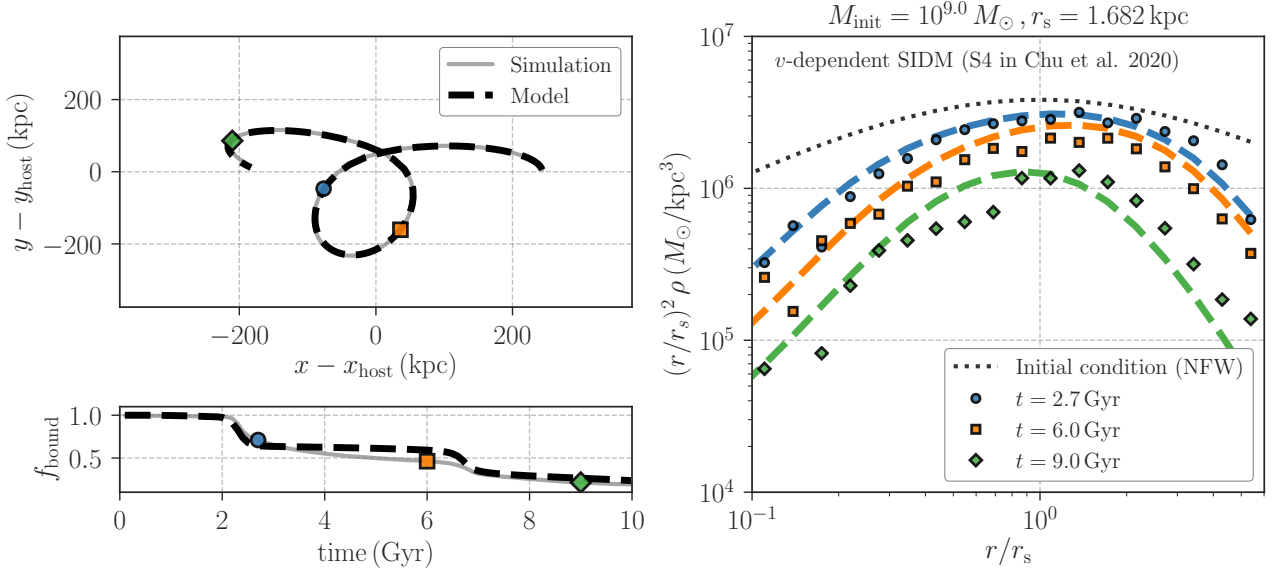


Figure 4. Similar to Figure 2, but we consider a velocity-dependent cross section given by Eq (14).

as a function of (x_c, η) . The blue circles in the figure represent the simulation results, while the solid lines show our model predictions. We assume $\mathcal{A} = 0.50$ for every model prediction in the figure. We find that our model can provide a reasonable fit to the simulation results with $\eta \gtrsim 0.35$ and a range of $0.6 \leq x_c \leq 1.5$, but a sizeable difference between the simulation results and our model can be found at an extreme value of $\eta \approx 0.05$. Note that orbits with $\eta \lesssim 0.2$ rarely happens in cosmological simulations of collision-less dark matter (e.g. Jiang et al. 2015). Even for the orbits at $\eta = 0.05$, our model can explain overall trends in the time evolution of the subhalo mass with a level of 20 – 30%.

4.2.3 Model precision of subhalo density profiles

We then investigate the subhalo density profiles at various initial conditions as well as examine the dependence on the self-interaction cross section σ/m . Figure 6 compares the subhalo density profiles in our N-body simulations with the model counterparts. In this figure, each panel contains nine different lines which show the fractional difference between the simulation results and our model predictions at different epochs of $t = 1.8, 2.7, 3.6, 4.5, 5.4, 6.3, 7.2, 8.1$ and 9.0 Gyr. Individual panels in the figure show the comparisons with different simulation setups.

At the first row, we show the results as varying σ/m for a fixed initial condition of the subhalo. We observe that our model can

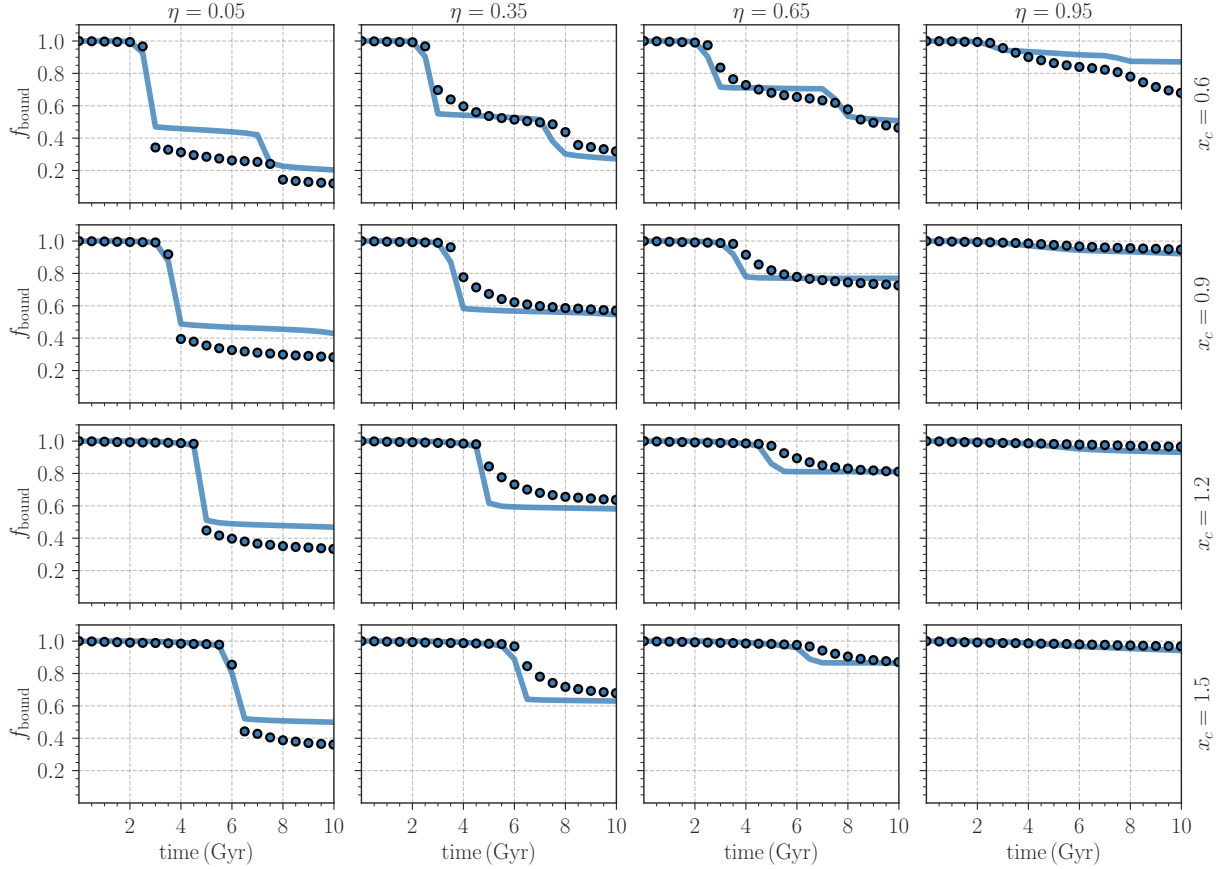


Figure 5. The mass evolution of infalling subhaloes at various orbits for the SIDM model with the velocity-independent cross section of $1 \text{ cm}^2/\text{g}$. In each panel, the blue circles show the simulation results, while the line presents our model prediction. The subhalo orbits are characterised by two parameters of x_c and η . The results with $\eta = 0.05, 0.35, 0.65,$ and 0.95 are shown from left to right, while we increase x_c as $x_c = 0.6, 0.9, 1.2,$ and 1.5 from top to bottom. Note that larger x_c corresponds to longer orbital period, and smaller η provides more radial orbits (see Subsection 2.1 for details).

reproduce the subhalo density profiles in the simulations with a level of ~ 0.2 dex in a range of $r/r_s \gtrsim 0.5$ when varied the cross section σ/m . The model precision becomes worse as we increase σ/m , implying that effects of gravothermal instability may be required to be revised for a better model.

Three panels at the second row summarise the comparisons at different orbital parameters (x_c, η) for the SIDM model with $\sigma/m = 1 \text{ cm}^2/\text{g}$. Except for the left panel at the second row, our model can provide an accurate fit to the simulation results. Note that the left panel at the second row assumes an extreme value of η corresponding to a highly elongated orbit around the host. For tidal effects, our model partly relies on the assumption of the subhalo on a circular orbit (Eq. 36). Hence the model would tend to be invalid for more radial orbits.

In the bottom panels in Figure 6, we can see the effect of initial conditions of subhaloes for the SIDM model with $\sigma/m = 1 \text{ cm}^2/\text{g}$. The left bottom panel shows the comparisons when we assume an initial subhalo density profile with a higher concentration, while the middle bottom panel presents the results with the subhalo with a lower concentration at $t = 0$. We find that our model can reproduce the simulation results with a level of ~ 0.2 dex for a wide range of the subhalo concentration at their initial density. The model precision

gets worse for the lower-concentration subhalo, indicating that a more detailed calibration of the gravothermal fluid model (see Eq. 20) and the tidal stripping model (see Eq. 41) are beneficial. The right bottom panel in the figure summarises the comparisons when we increase the subhalo mass at its initial state as $M_{\text{sub}} = 10^{10} M_\odot$. Although the model provides a good fit to the simulation results by ~ 5.4 Gyr, it fails to explain the subhalo density at outskirts in the simulations at later epochs. For the more massive subhalo, we find a difference of the time evolution of the subhalo mass between the simulation and the model prediction at $t \gtrsim 6$ Gyr. This difference can lead to the systematic offsets found in the right bottom panel in the figure, because the tidal evolution of the subhalo density profile would be well described by a function of the remaining bound mass at each moment (see Subsection 4.1). Hence, we expect that more detailed consideration of tidal effects can be relevant to a precise modelling of infalling subhaloes with their masses of $\gtrsim 10^{10} M_\odot$ in a MW-sized halo (e.g. self-friction effects as explored in Fujii et al. 2006; Fellhauer & Lin 2007).

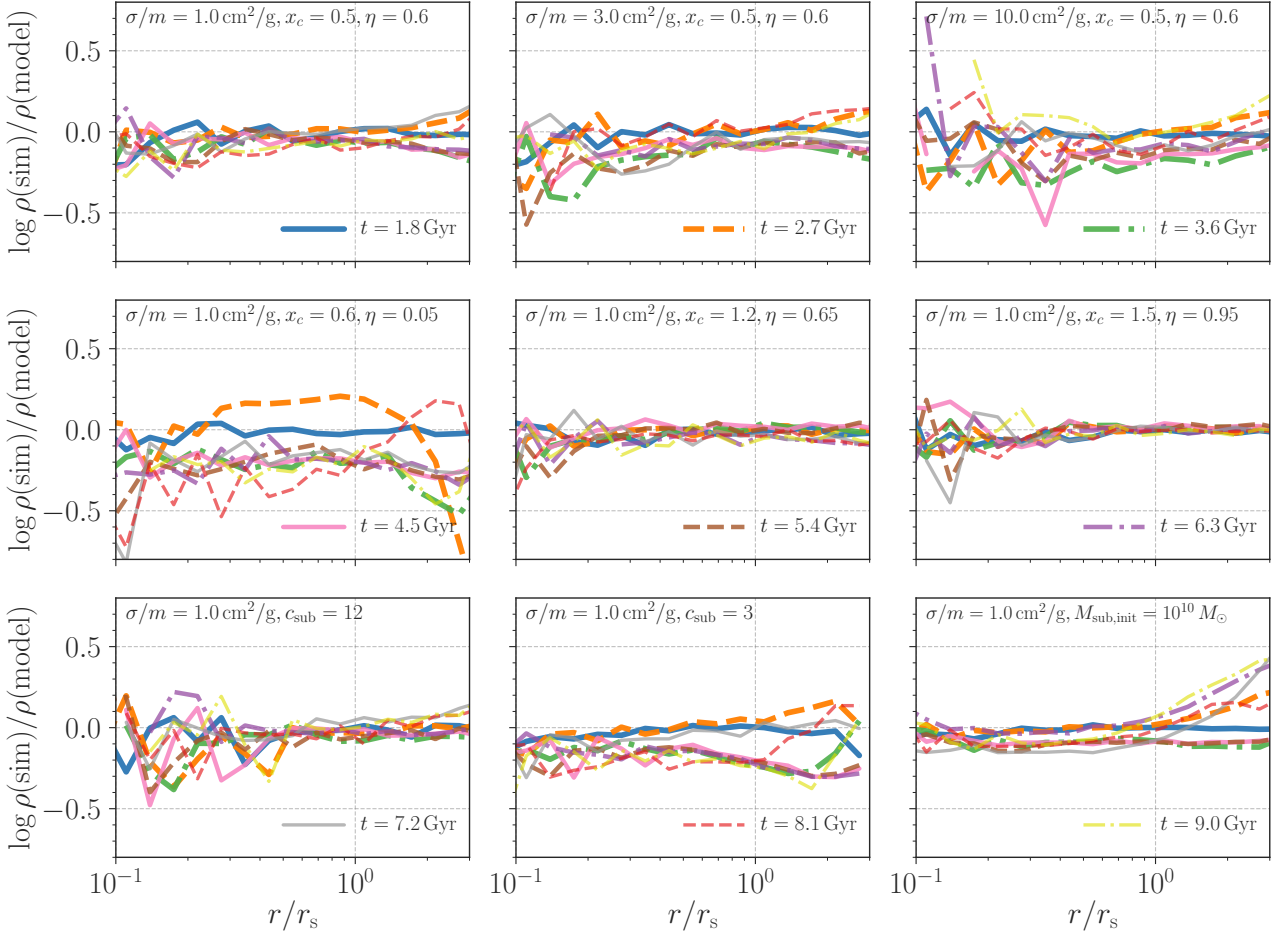


Figure 6. Precision of the subhalo density profile by our semi-analytic model. Each panel shows fractional differences between the density profile in our N-body simulations and the model prediction at different epochs of $t = 1.8, 2.7, 3.6, 4.5, 5.4, 6.3, 7.2, 8.1$ and 9 Gyr. At the first row, we show the comparison at a fixed subhalo orbit, but increase the cross section as $\sigma/m = 1, 3,$ and $10 \text{ cm}^2/\text{g}$ from left to right. At the second row, we fix the cross section to $\sigma/m = 1 \text{ cm}^2/\text{g}$, but change the subhalo orbits. At the third row, we examine different density profiles of subhaloes at $t = 0$ in the SIDM model with $\sigma/m = 1 \text{ cm}^2/\text{g}$.

4.3 Comparison with previous studies

In the aforementioned sections, we introduced a semi-analytic model of infalling subhaloes and made detailed comparisons with ideal N-body simulation results and the model predictions. We here discuss differences among our model and others in the literature.

4.3.1 Time evolution of density profiles of single SIDM haloes

Our model assumes a gravothermal fluid model based on the calibration of the thermal conductivity κ in Eq. (17) in Koda & Shapiro (2011), whereas we further include a correction based on our N-body simulations of isolated SIDM haloes as in Eq. (20). Previous studies have reported different models of κ for isolated and cosmological N-body simulations (e.g. Balberg et al. 2002; Koda & Shapiro 2011; Essig et al. 2019; Nishikawa et al. 2020). Also, the hydrostatic equilibrium (Eq. 15) is not always valid in SIDM haloes at small cross sections (e.g. Nishikawa et al. 2020). Hence, a correction of the gravothermal fluid model would be needed for a precise modelling of time evolution of SIDM density profiles.

For another approach, Robertson et al. (2021) introduced a mapping method from a given NFW profile to an isothermal density

profile based on Jeans equations, referred to as isothermal Jeans modelling. In the isothermal Jeans modelling, one assumes that a SIDM halo follows an isothermal density profile at the radius smaller than r_c , while the NFW profile remains unchanged at outer radii. The isothermal Jeans modelling is found to be valid when one predicts the density profile of a SIDM halo at a given epoch, but a proper choice of r_c is required to explain simulation results on a case-by-case basis. Hence, the isothermal Jeans modelling is less relevant to predicting the time evolution of the SIDM density profile.

4.3.2 Evolution of infalling subhaloes

Our model assumes that the motion of infalling SIDM subhaloes is governed by Eq. (26) as same as in Jiang et al. (2021a). The model of Jiang et al. (2021a), referred to as J21 model, assumes that (i) an isolated SIDM halo follows a cored profile with a characteristic core radius where every particle is expected to have interacted once within a time, (ii) a parameter of the mass loss in Eq. (33) is fixed to $\mathcal{A} = 0.55$ as expected in the collision-less dark matter (Green et al. 2021), and (iii) the mass loss by tidal stripping effects (Eq. 33) truncates the subhalo boundary radius and the mass loss by self-interactions (Eq. 38) decreases the amplitude in the subhalo density.

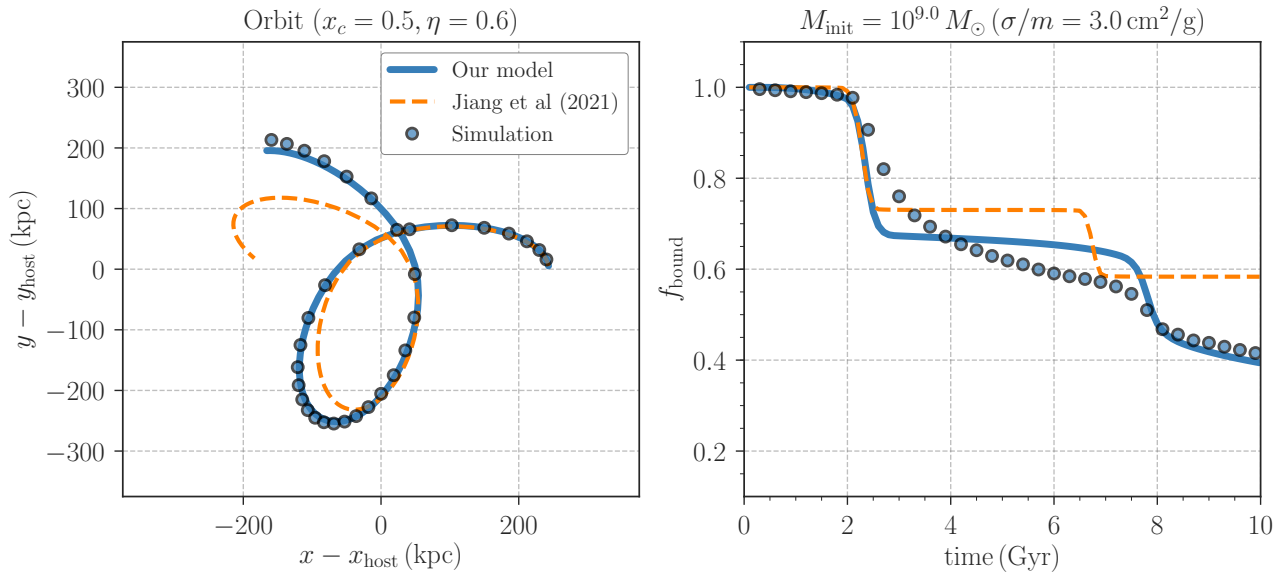


Figure 7. Similar to Figure 3, but we include the model prediction in Jiang et al. (2021a). In this figure, we assume a velocity-independent cross section of $\sigma/m = 3 \text{ cm}^2/\text{g}$. The blue circles show our simulation results, the solid lines are our model predictions, and the orange dashed lines represent the model in Jiang et al. (2021a).

We also refer the readers to a brief description of the J21 model in Appendix D.

Figure 7 summarises the comparison with the J21 model and ours for the SIDM with the cross section of $\sigma/m = 3 \text{ cm}^2/\text{g}$. We find that the difference in the subhalo orbit is mostly explained by a mismatch of the host halo density between the simulation result and the J21 model. On the time evolution of the subhalo mass, an appropriate choice of the parameter \mathcal{A} is needed to provide a better fit to our simulation results. Note that Jiang et al. (2021a) assumes a static NFW gravitational potential for the host halo in their analysis. Hence, the orbital evolution of infalling subhaloes in Jiang et al. (2021a) may be less affected by choices of the model, whereas the J21 model would have a 50%-level uncertainty in predicting the time evolution of the subhalo mass over ~ 10 Gyr.

Recently, Correa (2021) has developed a semi-analytic model of infalling subhaloes in a static host based on a gravothermal fluid model and derived an interesting constraint of SIDM models with observations of MW dwarf spheroidal galaxies. The model in Correa (2021) incorporated the gravothermal fluid model with the tidal evolution of subhaloes (van den Bosch et al. 2018; Green & van den Bosch 2019), accounting for the gravothermal collapse effects accelerated by the tidal stripping (Nishikawa et al. 2020; Sameie et al. 2020). However, the model computes the mass loss rate assuming a circular subhalo orbit and does not include the mass loss by the self-scattering-induced evaporation. This simplification can affect the subhalo mass at each moment. Because the gravothermal instability depends on how the subhalo mass density is tidally stripped, further developments would be interesting for a precise modelling of the gravothermal collapse effects in infalling subhaloes. Note that our model ignores the gravothermal instability induced by tidal stripping effects, while it can solve the orbital and structural evolution of subhaloes in a self-consistent way.

5 LIMITATIONS

Before concluding, we summarise the major limitations in our semi-analytic model of infalling subhaloes in a MW-sized host halo. The following issues will be addressed in future studies.

5.1 Baryonic effects

In this paper, we do not consider any baryonic effects. Baryons can affect our semi-analytic model in various ways.

The presence of stellar and gas components is common in most of real galaxies. The baryons at the galaxy centre can deepen the gravitational potential compared to dark-matter-only predictions. This allows an effective temperature of SIDM particles to have a flat or negative gradient in the radius, leading to decrease the size of SIDM core as well as increase the central SIDM density in baryon-dominated galaxies (Kaplinghat et al. 2014; Kamada et al. 2017b). These back-reaction effects between baryons and SIDM have been investigated in isolated N-body simulations (Sameie et al. 2018) and cosmological zoom-in simulations (Vogelsberger et al. 2014; Fitts et al. 2019; Robles et al. 2019; Sameie et al. 2021). Interestingly, the simulations in Sameie et al. (2018) showed that the SIDM core in a MW-sized halo can expand at early phases and contract later. This time variation can be important to predict orbits of infalling subhaloes in a realistic MW-sized galaxy.

In addition, the presence of stellar disc at the host centres can severely affect the mass loss of infalling subhaloes. D’Onghia et al. (2010) showed that subhaloes in the inner regions of the halo are efficiently destroyed in the presence of time-evolving stellar disc components, while Garrison-Kimmel et al. (2017) found that this suppression in the subhalo abundance can be explained by adding an embedded central disc potential to dark-matter-only simulations. Isolated N-body simulations also play important roles in studying the depletion of subhaloes in details (e.g Peñarrubia et al. 2010; Errani et al. 2017). Recently, Green et al. (2022) have explored the impact of a galactic disc potential on the subhalo populations in MW-like

haloes with their semi-analytic modelling. We expect that our semi-analytic model can be useful to investigate the effects of stellar disc components in the SIDM model by adding a stellar disc potential in the equation of motion (Eq. 26).

5.2 Gravothermal collapse

The gravothermal instability induces dynamical collapse of the SIDM core. This effect can be partly taken into account in our semi-analytic model with the gravothermal fluid model (see Subsection 3.1). Note that the gravothermal fluid model of isolated SIDM haloes predicts the core collapse over time, but it rarely happens within a Hubble time (e.g. Balberg et al. 2002). Our model still assumes that the gravothermal collapse occurs regardless of the tidal stripping effects, but this is not the case for some specific conditions (Nishikawa et al. 2020; Sameie et al. 2020). Nishikawa et al. (2020) found that the core collapse in the SIDM density can realise within a Hubble time for $\sigma/m \lesssim 10 \text{ cm}^2/\text{g}$ if the initial subhalo density is significantly truncated, while Sameie et al. (2020) showed that the evolution of the SIDM core is sensitive to the concentration in the initial subhalo density. Motivated by those findings, Correa (2021) developed a gravothermal fluid model of tidally stripped subhaloes with focus on a large self-interacting cross section of $20 - 150 \text{ cm}^2/\text{g}$. A calibration of the gravothermal fluid model in Correa (2021) with N-body simulations would be an interesting direction of future studies.

5.3 Comparisons with cosmological simulations

Our semi-analytic model has been calibrated with isolated N-body simulations. This indicates that our results may be affected by cosmological environments at the outermost radii. A lumpy and continuous mass accretion in an expanding universe can heat SIDM haloes, slowing the gravothermal core collapse. Detailed comparisons with our gravothermal fluid model of Eq. (20) with cosmological SIDM N-body simulations (e.g. Rocha et al. 2013; Elbert et al. 2015) can reveal how important environmental effects are in predicting time evolution of the SIDM density profiles.

The evolution of infalling subhaloes can be affected by other floating subhaloes in the host. The subhaloes should gravitationally interact with each other, and induce perturbations in the host gravitational potential. These complex effects might affect the orbital and structural evolution of infalling subhaloes. To examine these, it would be worth comparing our semi-analytic model with zoom-in simulation results of MW-sized cosmological haloes (e.g. Ebisu et al. 2022).

6 CONCLUSIONS AND DISCUSSIONS

In this paper, we have studied the evolution of a $10^9 M_\odot$ subhalo infalling onto a MW-sized host halo in the presence of self-interactions among dark matter particles. We have performed a set of ideal (dark-matter-only) N-body simulations of halo-subhalo mergers by varying self-interacting cross sections σ/m , subhalo orbits, and initial conditions of subhalo density profiles. For comparisons, we developed a semi-analytic model of infalling subhaloes in a given host halo by combining a gravothermal fluid model with subhalo mass losses due to tidal stripping and ram-pressure-induced effects. We then made detailed comparisons with our simulation results and the semi-analytic model, allowing to improve physical understanding of self-interacting dark matter (SIDM) substructures. Although our study imposes several assumptions, we gained meaningful insights as follows:

(i) In our N-body simulations for a range of $\sigma/m \lesssim 30 \text{ cm}^2/\text{g}$, the fluid model with the thermal conductivity calibrated in Koda & Shapiro (2011) can not explain the time evolution of the SIDM core in an isolated halo whose initial density follows a NFW profile. We provided a simple correction of the model as in Eq. (20). Our corrected gravothermal fluid model allows to predict the time evolution of SIDM density profiles over 10 Gyr with a 10%-level precision.

(ii) The structural evolution of infalling subhaloes can be explained by the prediction for collision-less dark matter as proposed in Green & van den Bosch (2019), even if we include the self-interaction of dark matter particles. The evaporation due to self-interacting ram pressure can not alter the SIDM density profile in isolation as long as the cross section is smaller than $\sigma/m \lesssim 10 \text{ cm}^2/\text{g}$. The tidal stripping effects play a central role in the change in the density profile of the SIDM subhalo across its orbit (Subsection 4.1). When the initial subhalo density is set to be consistent with the Λ CDM prediction at $z \sim 2$, the SIDM subhaloes do not undergo the gravothermal collapse over 10 Gyr in our simulations.

(iii) The orbit of SIDM subhaloes can be precisely predicted by a simple framework based on point-mass approximation incorporated with the dynamical friction (Chandrasekhar 1943) and the ram-pressure-induced deceleration (Kummer et al. 2018) (Subsection 3.2). It would be worth noting that a precise modelling of time-evolving host halo density is essential to reproduce our N-body simulation results.

(iv) The time evolution of SIDM subhalo masses can be also explained by a common method accounting for the mass loss due to tidal stripping and ram-pressure effects (Subsection 3.3). Our N-body simulations need an effective mass loss rate of the tidal stripping (Eq. 33) to depend on the self-interacting cross section σ/m , that is a new systematic effect in the prediction of SIDM subhaloes.

(v) Our semi-analytic model can provide a reasonable fit to the simulation results for various cross sections (including a velocity-dependent scenario as in Eq. 14), subhalo orbits, and initial subhalo density profiles. A typical uncertainty in the model prediction is 0.1-0.2 dex for the SIDM subhalo density profiles over 10 Gyr in a range of $\sigma/m \lesssim 10 \text{ cm}^2/\text{g}$.

Our semi-analytic model provides a simple, efficient, and physically-intuitive prediction of SIDM subhaloes, but it has to be revised in various aspects for applications to real data sets. The model should include more realistic effects, such as baryonic effects in a MW-sized host halo, the gravothermal instability induced by tidal stripping effects, cosmological mass accretion around the host halo, and gravitational interaction among subhaloes in the host (see Section 5 for details). We expect the model to be improved on a step-by-step basis with a use of cosmological N-body simulations as well as isolated N-body simulations including baryonic components in the host gravitational potential. This is along the line of our ongoing study.

ACKNOWLEDGEMENTS

The authors thank Kohei Hayashi and Ayuki Kamada for useful discussions about modelling of SIDM haloes at early stages of this work. This work is supported by MEXT/JSPS KAKENHI Grant Numbers (19K14767, 19H01931, 20H05850, 20H05861, 21H04496). Numerical computations were in part carried out on Cray XC50 at Center for Computational Astrophysics, National Astronomical Observatory of

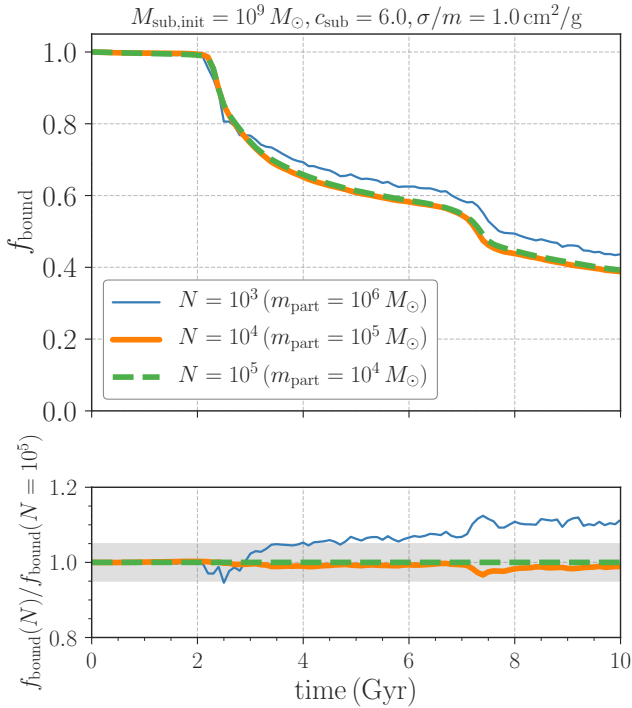


Figure A1. Convergence tests for evolution of subhalo bound mass. The top panel shows the fraction of subhalo bound mass (normalised to unity at $t = 0$) when we vary the particle resolution in our simulations. The bottom panel represents the fractional difference among the simulation results. The grey shaded region in the bottom shows a $\pm 5\%$ difference. In each panel, the blue thin, orange thick, green dashed lines stand for the simulation results with $m_{\text{part}} = 10^6$, 10^5 and $10^4 M_{\odot}$, respectively. This figure highlights that our fiducial run with $m_{\text{part}} = 10^5 M_{\odot}$ shows a converged result within a few percents.

Japan, Oakforest-PACS at the CCS, University of Tsukuba, and the computer resource offered under the category of General Project by Research Institute for Information Technology, Kyushu University.

DATA AVAILABILITY

The data underlying this article will be shared on reasonable request to the corresponding author.

APPENDIX A: CONVERGENCE TESTS FOR N-BODY SIMULATIONS

We here summarise convergence tests of our N-body simulations for halo-subhalo mergers. In this Appendix, we work on the same parameter sets as “SIDM1” in Table 1. We run three different N-body simulations with the particle mass of m_{part} being 10^4 , 10^5 and $10^6 M_{\odot}$, respectively. In each simulation, we set the gravitational softening length as in Eq (13). Note that the host halo (subhalo at $t = 0$) can be resolved with 10^8 (10^5), 10^7 (10^4), and 10^6 (10^3) when we set $m_{\text{part}} = 10^4$, 10^5 and $10^6 M_{\odot}$.

Figures A1 and A2 summarise the convergence tests in our N-body simulations. We found that our fiducial set up with $m_{\text{part}} = 10^5 M_{\odot}$ can make the subhalo mass evolution converged within a 2–3% level, while the subhalo density profile at $r/r_s \gtrsim 0.3$ in our simulations

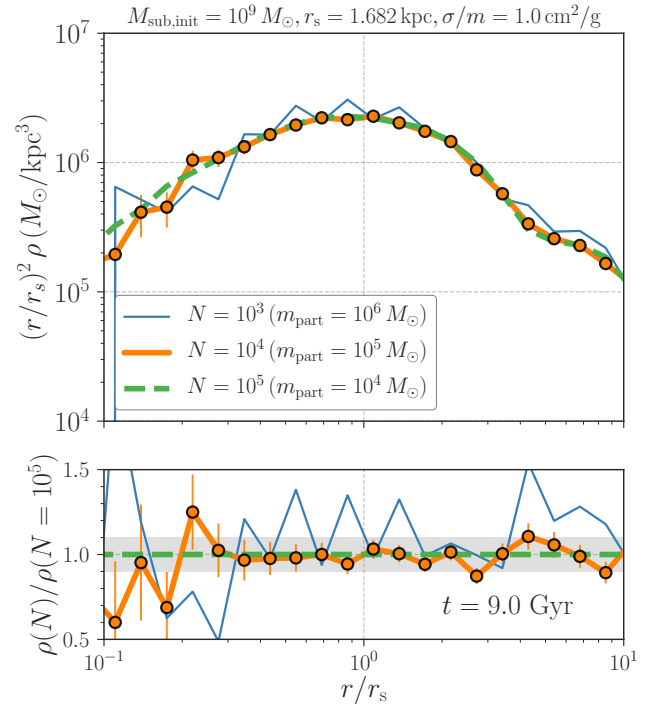


Figure A2. Convergence tests for subhalo density profiles. Similar legends are applied as in Figure A1. The top panel shows the subhalo density profiles evolved by 9 Gyr when the resolution is varied, while the bottom represents the fractional difference. The grey region in the bottom panel highlights a $\pm 10\%$ difference.

looks converged with a 10%-level precision. We caution that the inner subhalo profile may suffer from some numerical resolution effects in our simulation sets.

APPENDIX B: CALIBRATION OF GRAVOTHERMAL FLUID MODEL FOR AN ISOLATED HALO

In this Appendix, we describe our calibration of the gravothermal fluid model. For the calibration, we perform N-body simulations of an isolated halo with its initial density profile following a NFW profile as varying the self-interacting cross section σ/m . In these isolated simulations, we set the halo mass and the scaled radius at $t = 0$ to be $10^{12} M_{\odot}$ and $r_s = 21.18$ kpc. We examine five cross sections of $\sigma/m = 0.3, 1, 3, 10$ and $30 \text{ cm}^2/\text{g}$ and evolve the halo by 10 Gyr in our simulations. The simulation outputs are stored with a time interval of 0.1 Gyr, producing 100 snapshots for a given SIDM model. We refer the readers to Subsection 2.1 about how to prepare an isolated NFW halo.

Figure B1 summarises the comparison of the SIDM density profile between the simulation results and the gravothermal fluid model in Koda & Shapiro (2011). In the figure, we show the density profiles at a dimensionless epoch $t/t_0 = 3$, where t_0 is given by Eq. (25). Once considering evolution with respect to dimensionless epochs t/t_0 , we find that the gravothermal fluid model predicts almost an identical density profile at a given t/t_0 regardless of the exact value of σ/m . The gravothermal fluid prediction is shown by the solid line in the top panel of figure B1, while different coloured symbols represent our simulation results at $t/t_0 = 3$. Although the simulation results

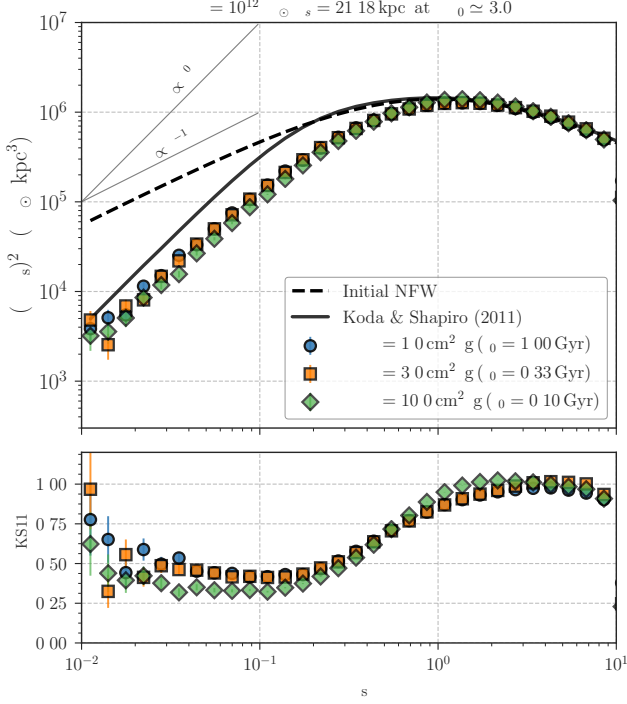


Figure B1. SIDM density profiles as a function of the cross section σ/m . In the upper panel, the solid line shows the gravothermal fluid model with the heat conductivity calibrated in [Koda & Shapiro \(2011\)](#), while different coloured symbols represent our N-body simulation results for an isolated halo with its mass of $10^{12} M_{\odot}$. We show the simulation results at a dimensionless time $t/t_0 = 3$, where t_0 is a characteristic relaxation time scale given in Eq. (25). Because the time scale t_0 depends on σ/m , each symbol represents the density profile at different epoch; The blue circle shows the density profile at $t \approx 3$ Gyr for the SIDM with $\sigma/m = 1 \text{ cm}^2/\text{g}$, while the orange square and green diamond show the counterparts at $t \approx 1$ Gyr and $t \approx 0.3$ Gyr for $\sigma/m = 3 \text{ cm}^2/\text{g}$ and $10 \text{ cm}^2/\text{g}$, respectively. Note that the upper panel shows the quantity of $\sim r^2 \rho$. For ease of comparisons, we also show the initial NFW profile by the dashed line in the top panel. The bottom panel shows the fractional difference between the gravothermal fluid model and the simulation results at $t/t_0 = 3$, highlighting that a universal correction can be applied to the gravothermal fluid prediction for various σ/m .

exhibit a $O(10)\%$ difference from the gravothermal fluid model at $r/r_s \approx 0.1$, the difference is found to be almost independent on σ/m if comparing the density profiles at the same dimensionless epoch t/t_0 . This finding motivates us to develop a correction function of the gravothermal fluid model below;

$$\rho_{\text{SIDM}}(r, t, \sigma/m) = \rho_{\text{gt}}(r, t, \sigma/m) C(r/r_s, t/t_0), \quad (\text{B1})$$

where C represents the correction function which we would like to find. After some trials, we find that our simulation results can be well explained by a four-parameter function below;

$$C(x, \tilde{t}) = \frac{N(x^{\beta} + \alpha^{\beta})}{(x + \gamma)^{\beta}}, \quad (\text{B2})$$

where $x = r/r_s$ and we assume that N , α , β and γ depend on $\tilde{t} = t/t_0$.

Using the density profile of the simulated halo at a given snapshot and cross section of σ/m , we find the best-fit parameters of N , α , β and γ by minimising the chi-square value of

$$\chi^2 = \sum_i [\rho_{\text{sim}}(r_i, t, \sigma/m) - \rho_{\text{SIDM}}(r_i, t, \sigma/m)]^2, \quad (\text{B3})$$

where ρ_{sim} represents the density profile of the simulated halo and r_i is the i -th bin in the halo-centric radius. For this chi-square analysis, we perform a logarithmic binning in r/r_s with the number of bins being 35 in a range of $0.01 < r/r_s < 30$ when computing the spherical density profile of the simulated halo. After finding the best-fit parameters for a given set of snapshot time t and cross section σ/m , we derive the t/t_0 -dependence as in Eqs. (21)-(24). Figure B2 summarises our calibration, demonstrating that the model of Eq. (20) can provide a good fit to the simulation results for a wide range of σ/m and t . We confirm that our calibrated model has a 10%-level precision in the range of $t/t_0 \lesssim 100$. It would be worth noting that our model has been calibrated for a specific initial condition. Hence, our model can not be applied to general cases, but it would provide a reasonable fit to the SIDM density profile as long as its initial density follows a NFW profile.

APPENDIX C: A FITTING FORMULA OF THE TRANSFER FUNCTION FOR TIDALLY TRUNCATED DENSITY PROFILES

In this appendix, we provide a fitting formula of the transfer function developed in [Green & van den Bosch \(2019\)](#). In the context of tidal evolution of collision-less dark matter subhaloes, the transfer function is commonly defined as

$$H(r, t) = \frac{\rho(r, t)}{\rho(r, t=0)}, \quad (\text{C1})$$

where H is the transfer function, r is the radius from the centre of the subhalo, and $\rho(r, t)$ is the subhalo density profile at an epoch of t . Using a set of collision-less N-body simulations of minor mergers, [Green & van den Bosch \(2019\)](#) found that H can be well approximated as the form below;

$$H(r, t) = \frac{f_{\text{te}}}{1 + \left(\tilde{r} \left[\frac{\tilde{r}_{\text{sub, vir}} - \tilde{r}_{\text{te}}}{\tilde{r}_{\text{sub, vir}} \tilde{r}_{\text{te}}} \right] \right)^{\delta}}, \quad (\text{C2})$$

where $\tilde{r} = r/r_{s, \text{init}}$ such that all radii in Eq. (C2) are normalized to the initial NFW scale radius of the subhalo $r_{s, \text{init}}$.

Eq. (C2) contains three model parameters and those depend on the initial subhalo concentration c_{sub} and the bound mass fraction of the subhalo at the epoch t (denoted as f_b). Throughout this paper, we adopt

$$f_{\text{te}} = f_b^{a_1} (c_{\text{sub}, 10})^{a_2} c_{\text{sub}}^{a_3} (1-f_b)^{a_4}, \quad (\text{C3})$$

$$\tilde{r}_{\text{te}} = \tilde{r}_{\text{sub, vir}} f_b^{b_1} (c_{\text{sub}, 10})^{b_2} c_{\text{sub}}^{b_3} (1-f_b)^{b_4} \times \exp \left[b_5 (c_{\text{sub}, 10})^{b_6} (1-f_b) \right], \quad (\text{C4})$$

$$\delta = c_0 f_b^{c_1} (c_{\text{sub}, 10})^{c_2} c_{\text{sub}}^{c_3} (1-f_b)^{c_4}, \quad (\text{C5})$$

where $c_{\text{sub}, 10} = c_{\text{sub}}/10$, $a_1 = 0.338$, $a_2 = 0.000$, $a_3 = 0.157$, $a_4 = 1.337$, $b_1 = 0.448$, $b_2 = 0.272$, $b_3 = -0.199$, $b_4 = 0.011$, $b_5 = -1.119$, $b_6 = 0.093$, $c_0 = 2.779$, $c_1 = -0.035$, $c_2 = -0.337$, $c_3 = -0.099$, and $c_4 = 0.415$. Note that the function in Eq. (C2) has been calibrated for the collision-less dark matter. Hence, we have tested if it can be applied to collisional scenarios in Subsection 4.1.

APPENDIX D: A SEMI-ANALYTIC MODEL IN JIANG ET AL. (2021A)

For the sake of clarity, we here summarise a semi-analytic model in [Jiang et al. \(2021a\)](#). The model assumes that an isolated SIDM halo

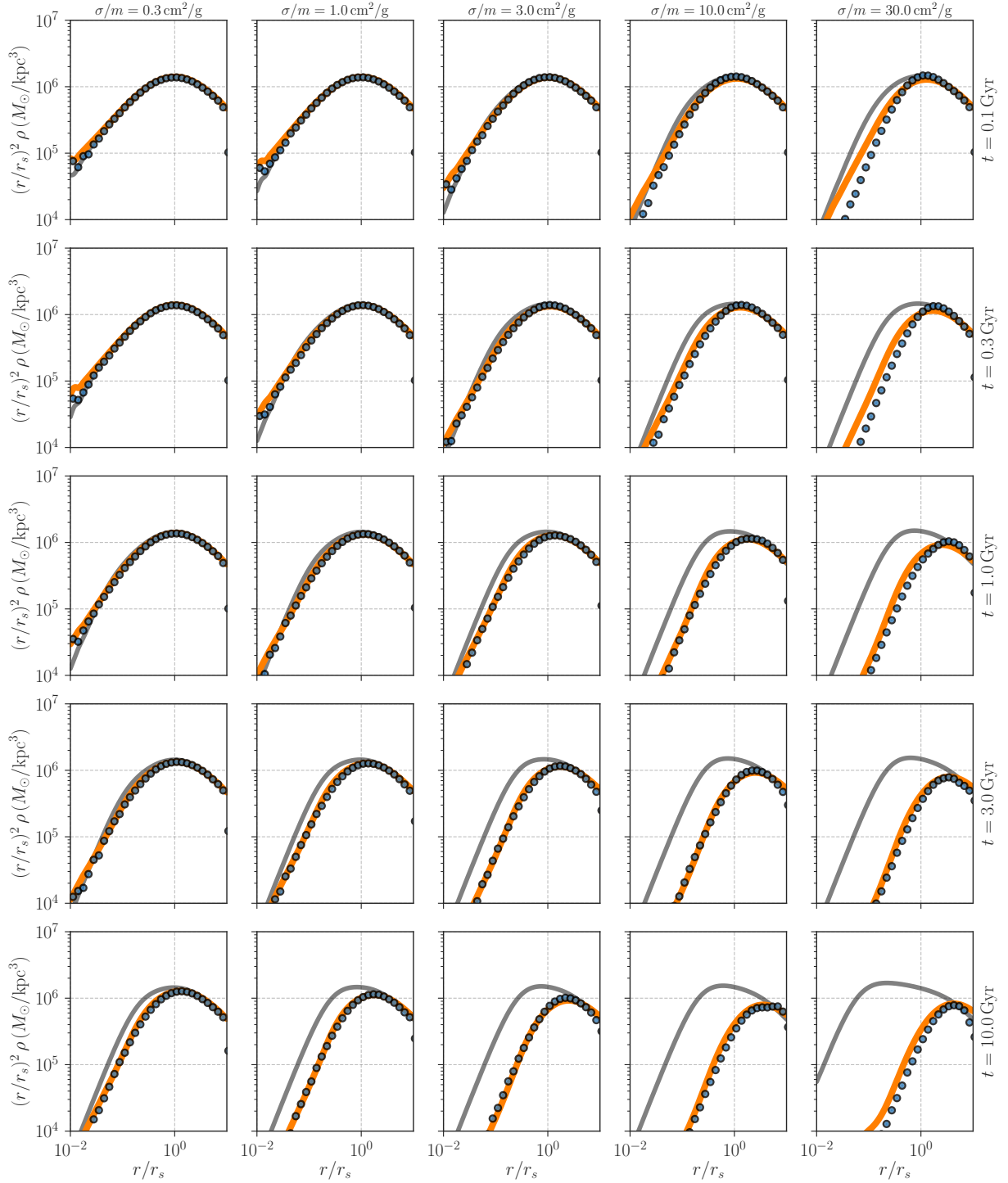


Figure B2. Tests of our calibrated gravothermal fluid model (Eq. 20) against the N-body simulations of an isolated halo. In each panel, the blue circles show the simulation results, while the grey and orange lines represent the model in Koda & Shapiro (2011) and our calibrated model, respectively. From left to right (top to bottom), we show the comparisons as increasing σ/m (epoch t).

follows a NFW profile at its initial state and the density profile at a given age t can be approximated as

$$\rho_{\text{SIDM,J21}}(r) = \frac{1}{4\pi r^2} \frac{dM_{\text{SIDM,J21}}}{dr}, \quad (\text{D1})$$

$$M_{\text{SIDM,J21}}(r) = \tanh\left(\frac{r}{r_c}\right) M_{\text{NFW}}(r), \quad (\text{D2})$$

where $M_{\text{NFW}}(r)$ is the enclosed mass of the initial NFW profile, and r_c represents an effective core radius of the SIDM halo and depends on the time of t . To be specific, r_c is given by $\min[0.5r_1, r_s]$ (r_s is the scaled radius for the initial NFW profile) and r_1 is set by

$$\langle \sigma v/m \rangle \rho_{\text{SIDM,J21}}(r_1) t = 1, \quad (\text{D3})$$

where the above equation means that the SIDM core size can be related to the radius where every SIDM particle has interacted once by the time t . The average in Eq. (D3) is given by

$$\langle \sigma v / m \rangle = \int_0^\infty dv v \frac{\sigma}{m} f(v; v_c), \quad (\text{D4})$$

where $f(v; v_c)$ is the Maxwell-Boltzmann distribution of Eq. (45). The parameter v_c is set to $4\sigma_{v,J21}(r)/\sqrt{\pi}$ with

$$\sigma_{v,J21}^2(r) = \frac{1}{\rho_{\text{SIDM},J21}(r)} \int_r^\infty dr' \frac{\rho_{\text{SIDM},J21}(r')}{r'} \frac{GM_{\text{SIDM},J21}(r')}{r'}. \quad (\text{D5})$$

In Jiang et al. (2021a), the authors solve the orbital evolution of infalling subhaloes as same as in Subsection 3.2. The mass loss due to the tidal stripping is also set by Eq. (33), but they adopt $\mathcal{A} = 0.55$ and $q = 1$ for any SIDM models. They also take into account the mass loss by the self-interacting evaporation as in Eq. (38). For a given mass loss rate, the model in Jiang et al. (2021a) then updates the subhalo density profile after a finite time of Δt by rules below;

$$M_{\text{sub}}(\rho_0, r'_{\text{out}}) - M_{\text{sub}}(\rho_0, r_{\text{out}}) = \left(\frac{dM_{\text{sub}}}{dt} \right)_{\text{TS}} \Delta t, \quad (\text{D6})$$

$$M_{\text{sub}}(\rho'_0, r_{\text{out}}) - M_{\text{sub}}(\rho_0, r_{\text{out}}) = \left(\frac{dM_{\text{sub}}}{dt} \right)_{\text{RPe}} \Delta t, \quad (\text{D7})$$

where $M_{\text{sub}}(\rho_0, r_{\text{out}})$ is the enclosed mass of the subhalo at its boundary radius of r_{out} with the density amplitude being ρ_0 . We denote r'_{out} and ρ'_0 as the quantities to be updated. Eqs. (D6) and (D7) are designed so that the tidal stripping can remove the subhalo mass at its outermost radius, while the ram-pressure effects can affect the overall subhalo density profile.

REFERENCES

- Alam S., et al., 2021, *Phys. Rev. D*, **103**, 083533
 Ando S., Ishiyama K., 2015, *J. Cosmology Astropart. Phys.*, **2015**, 024
 Balberg S., Shapiro S. L., Inagaki S., 2002, *ApJ*, **568**, 475
 Baur J., Palanque-Delabrouille N., Yèche C., Magneville C., Viel M., 2016, *J. Cosmology Astropart. Phys.*, **2016**, 012
 Bond J. R., Cole S., Efstathiou G., Kaiser N., 1991, *ApJ*, **379**, 440
 Bullock J. S., Boylan-Kolchin M., 2017, *ARA&A*, **55**, 343
 Chandrasekhar S., 1943, *ApJ*, **97**, 255
 Chu X., Garcia-Cely C., Murayama H., 2020, *J. Cosmology Astropart. Phys.*, **2020**, 043
 Correa C. A., 2021, *MNRAS*, **503**, 920
 Creasey P., Sameie O., Sales L. V., Yu H.-B., Vogelsberger M., Zavala J., 2017, *MNRAS*, **468**, 2283
 D'Onghia E., Springel V., Hernquist L., Keres D., 2010, *ApJ*, **709**, 1138
 Diemer B., Kravtsov A. V., 2015, *ApJ*, **799**, 108
 Dvorkin C., Blum K., Kamionkowski M., 2014, *Phys. Rev. D*, **89**, 023519
 Ebisu T., Ishiyama T., Hayashi K., 2022, *Phys. Rev. D*, **105**, 023016
 Elbert O. D., Bullock J. S., Garrison-Kimmel S., Rocha M., Oñorbe J., Peter A. H. G., 2015, *MNRAS*, **453**, 29
 Errani R., Peñarrubia J., Laporte C. F. P., Gómez F. A., 2017, *MNRAS*, **465**, L59
 Essig R., McDermott S. D., Yu H.-B., Zhong Y.-M., 2019, *Phys. Rev. Lett.*, **123**, 121102
 Fellhauer M., Lin D. N. C., 2007, *MNRAS*, **375**, 604
 Fitts A., et al., 2019, *MNRAS*, **490**, 962
 Fujii M., Funato Y., Makino J., 2006, *PASJ*, **58**, 743
 Garrison-Kimmel S., et al., 2017, *MNRAS*, **471**, 1709
 Gingold R. A., Monaghan J. J., 1977, *MNRAS*, **181**, 375
 Green S. B., van den Bosch F. C., 2019, *MNRAS*, **490**, 2091
 Green S. B., van den Bosch F. C., Jiang F., 2021, *MNRAS*, **503**, 4075
 Green S. B., van den Bosch F. C., Jiang F., 2022, *MNRAS*, **509**, 2624
 Hayashi K., Chiba M., Ishiyama T., 2020, *ApJ*, **904**, 45
 Hayashi K., Ibe M., Kobayashi S., Nakayama Y., Shirai S., 2021, *Phys. Rev. D*, **103**, 023017
 Hopkins P. F., 2015, *MNRAS*, **450**, 53
 Ishiyama T., et al., 2013, *ApJ*, **767**, 146
 Jiang L., Cole S., Sawala T., Frenk C. S., 2015, *MNRAS*, **448**, 1674
 Jiang F., Kaplinghat M., Lisanti M., Slone O., 2021a, arXiv e-prints, p. arXiv:2108.03243
 Jiang F., Dekel A., Freundlich J., van den Bosch F. C., Green S. B., Hopkins P. F., Benson A., Du X., 2021b, *MNRAS*, **502**, 621
 Kamada A., Kohri K., Takahashi T., Yoshida N., 2017a, *Phys. Rev. D*, **95**, 023502
 Kamada A., Kaplinghat M., Pace A. B., Yu H.-B., 2017b, *Phys. Rev. Lett.*, **119**, 111102
 Kaplinghat M., Keeley R. E., Linden T., Yu H.-B., 2014, *Phys. Rev. Lett.*, **113**, 021302
 Kaplinghat M., Tulin S., Yu H.-B., 2016, *Phys. Rev. Lett.*, **116**, 041302
 Kaplinghat M., Valli M., Yu H.-B., 2019, *MNRAS*, **490**, 231
 Kaplinghat M., Ren T., Yu H.-B., 2020, *J. Cosmology Astropart. Phys.*, **2020**, 027
 Kawasaki M., Nakatsuka H., Nakayama K., Sekiguchi T., 2021, *J. Cosmology Astropart. Phys.*, **2021**, 015
 Kim S. Y., Peter A. H. G., 2021, arXiv e-prints, p. arXiv:2106.09050
 King I., 1962, *AJ*, **67**, 471
 Klypin A., Gottlöber S., Kravtsov A. V., Khokhlov A. M., 1999, *ApJ*, **516**, 530
 Koda J., Shapiro P. R., 2011, *MNRAS*, **415**, 1125
 Kummer J., Kahlhoefer F., Schmidt-Hoberg K., 2018, *MNRAS*, **474**, 388
 Lacey C., Cole S., 1993, *MNRAS*, **262**, 627
 Lokas E. L., Mamon G. A., 2001, *MNRAS*, **321**, 155
 Lovell M. R., Hellwing W., Ludlow A., Zavala J., Robertson A., Fattahi A., Frenk C. S., Hardwick J., 2020, *MNRAS*, **498**, 702
 Lucy L. B., 1977, *AJ*, **82**, 1013
 Lynden-Bell D., Eggleton P. P., 1980, *MNRAS*, **191**, 483
 Markevitch M., Gonzalez A. H., Clowe D., Vikhlinin A., Forman W., Jones C., Murray S., Tucker W., 2004, *ApJ*, **606**, 819
 Miki Y., Umemura M., 2018, *MNRAS*, **475**, 2269
 Nadler E. O., et al., 2021, *Phys. Rev. Lett.*, **126**, 091101
 Navarro J. F., Frenk C. S., White S. D. M., 1997, *ApJ*, **490**, 493
 Nishikawa H., Boddy K. K., Kaplinghat M., 2020, *Phys. Rev. D*, **101**, 063009
 Ogiya G., van den Bosch F. C., Hahn O., Green S. B., Miller T. B., Burkert A., 2019, *MNRAS*, **485**, 189
 Oman K. A., et al., 2015, *MNRAS*, **452**, 3650
 Orkney M. D. A., et al., 2021, *MNRAS*, **504**, 3509
 Palanque-Delabrouille N., Yèche C., Schöneberg N., Lesgourgues J., Walther M., Chabanier S., Armengaud E., 2020, *J. Cosmology Astropart. Phys.*, **2020**, 038
 Peñarrubia J., Benson A. J., Walker M. G., Gilmore G., McConnachie A. W., Mayer L., 2010, *MNRAS*, **406**, 1290
 Planck Collaboration et al., 2020, *A&A*, **641**, A6
 Pollack J., Spergel D. N., Steinhardt P. J., 2015, *ApJ*, **804**, 131
 Read J. I., Goerdt T., Moore B., Pontzen A. P., Stadel J., Lake G., 2006, *MNRAS*, **373**, 1451
 Reif F., 1965, *Fundamentals of Statistical and Thermal Physics*
 Ren T., Kwa A., Kaplinghat M., Yu H.-B., 2019, *Physical Review X*, **9**, 031020
 Robertson A., Massey R., Eke V., Schaye J., Theuns T., 2021, *MNRAS*, **501**, 4610
 Robles V. H., Kelley T., Bullock J. S., Kaplinghat M., 2019, *MNRAS*, **490**, 2117
 Rocha M., Peter A. H. G., Bullock J. S., Kaplinghat M., Garrison-Kimmel S., Oñorbe J., Moustakas L. A., 2013, *MNRAS*, **430**, 81
 Sameie O., Creasey P., Yu H.-B., Sales L. V., Vogelsberger M., Zavala J., 2018, *MNRAS*, **479**, 359
 Sameie O., Yu H.-B., Sales L. V., Vogelsberger M., Zavala J., 2020, *Phys. Rev. Lett.*, **124**, 141102
 Sameie O., et al., 2021, *MNRAS*, **507**, 720
 Santos-Santos I. M. E., et al., 2020, *MNRAS*, **495**, 58

- Shirasaki M., Macias O., Horiuchi S., Shirai S., Yoshida N., 2016, *Phys. Rev. D*, **94**, 063522
- Silverman M., Bullock J. S., Kaplinghat M., Robles V. H., Valli M., 2022, arXiv e-prints, p. [arXiv:2203.10104](https://arxiv.org/abs/2203.10104)
- Slatyer T. R., Wu C.-L., 2017, *Phys. Rev. D*, **95**, 023010
- Spergel D. N., Steinhardt P. J., 2000, *Phys. Rev. Lett.*, **84**, 3760
- Takada M., et al., 2014, *PASJ*, **66**, R1
- Tulin S., Yu H.-B., 2018, *Phys. Rep.*, **730**, 1
- Valli M., Yu H.-B., 2018, *Nature Astronomy*, **2**, 907
- Vogelsberger M., Zavala J., Loeb A., 2012, *MNRAS*, **423**, 3740
- Vogelsberger M., Zavala J., Simpson C., Jenkins A., 2014, *MNRAS*, **444**, 3684
- Weinberg M. D., 1994a, *AJ*, **108**, 1398
- Weinberg M. D., 1994b, *AJ*, **108**, 1403
- Weinberg M. D., 1997, *ApJ*, **478**, 435
- Xu W. L., Dvorkin C., Chael A., 2018, *Phys. Rev. D*, **97**, 103530
- Zavala J., Lovell M. R., Vogelsberger M., Burger J. D., 2019, *Phys. Rev. D*, **100**, 063007
- van den Bosch F. C., Ogiya G., 2018, *MNRAS*, **475**, 4066
- van den Bosch F. C., Ogiya G., Hahn O., Burkert A., 2018, *MNRAS*, **474**, 3043
- von Hoerner S., 1957, *ApJ*, **125**, 451

This paper has been typeset from a $\text{\TeX}/\text{\LaTeX}$ file prepared by the author.